

A 3D spectral anelastic hydrodynamic code for shearing, stratified flows

Joseph A. Barranco^{a,*}, Philip S. Marcus^b

^a *Kavli Institute for Theoretical Physics, University of California, Santa Barbara, CA 93106, USA*

^b *Department of Mechanical Engineering, University of California, Berkeley, CA 94720, USA*

Received 2 September 2005; received in revised form 12 March 2006; accepted 13 March 2006

Available online 4 May 2006

Abstract

We have developed a three-dimensional (3D) spectral hydrodynamic code to study vortex dynamics in rotating, shearing, stratified systems (e.g., the atmosphere of gas giant planets, protoplanetary disks around newly forming protostars). The time-independent background state is stably stratified in the vertical direction and has a unidirectional linear shear flow aligned with one horizontal axis. Superposed on this background state is an unsteady, subsonic flow that is evolved with the Euler equations subject to the anelastic approximation to filter acoustic phenomena. A Fourier–Fourier basis in a set of quasi-Lagrangian coordinates that advect with the background shear is used for spectral expansions in the two horizontal directions. For the vertical direction, two different sets of basis functions have been implemented: (1) Chebyshev polynomials on a truncated, finite domain, and (2) rational Chebyshev functions on an infinite domain. Use of this latter set is equivalent to transforming the infinite domain to a finite one with a cotangent mapping, and using cosine and sine expansions in the mapped coordinate. The nonlinear advection terms are time-integrated explicitly, the pressure/enthalpy terms are integrated semi-implicitly, and the Coriolis force and buoyancy terms are treated semi-analytically. We show that internal gravity waves can be damped by adding new terms to the Euler equations. The code exhibits excellent parallel performance with the message passing interface (MPI). As a demonstration of the code, we simulate the merger of two 3D vortices in the midplane of a protoplanetary disk.

© 2006 Elsevier Inc. All rights reserved.

PACS: 02.70.Hm; 47.11.+j; 47.32.Cc

Keywords: Hydrodynamics; Vortex dynamics; Anelastic approximation; Rotating flows; Stratified flows; Shear flows; Spectral methods; Coordinate mapping; Infinite domain

* Corresponding author. Current address: Theory Division, Harvard-Smithsonian Center for Astrophysics, 60 Garden St., MS-51, Cambridge, MA 02138, USA. Tel.: +1 617 495 7296; fax: +1 617 495 7093.

E-mail addresses: jbarranco@cfa.harvard.edu (J.A. Barranco), pmarcus@me.berkeley.edu (P.S. Marcus).

¹ NSF Astronomy and Astrophysics Postdoctoral Fellow.

1. Introduction

Three of Jupiter’s notable features are: rapid rotation (spin period of just under 10 h); an atmosphere striped with a large number of alternating zones and belts corresponding to strongly shearing east–west winds (hundreds of m/s); and many long-lived, coherent vortices, the most prominent being the great red spot (GRS). Of course, these three characteristics – rotation, shear, and vortices – are all dynamically linked, so much so that it is often claimed that the presence of the first two implies the likely existence of the third [31,32]. Protoplanetary disks (the disks of gas and dust in orbit around newly-forming protostars) also have rapid rotation and intense shear, which has inspired proposals that such disks should also be populated with long-lived, coherent storms [1,5–8]. These vortices may play two critical roles in star and planet formation: (1) In cool, non-magnetized disks, vortices may transport angular momentum radially outward so that mass can continue to accrete onto the growing protostar, and (2) vortices are very efficient at capturing and concentrating dust particles, which may help in the formation of planetesimals, the basic “building blocks” of planets.

Motivated by these geophysical and astrophysical problems, we have developed a three-dimensional (3D) spectral hydrodynamic code that employs specially tailored algorithms to handle the computational challenges due to rapid rotation, intense shear, and strong stratification. In subsonic flow, short-wavelength acoustic waves have periods that are much shorter than the characteristic timescale of the large-scale advective motions. In numerical simulations, the timestep for an explicit algorithm must be short enough to temporally resolve these fast waves (i.e., the Courant–Friedrich–Lewy, or CFL, condition), which may be inefficient for calculating the evolution of the slower, large-scale flow for long integration times. One strategy is to filter sound waves from the fluid equations (“sound-proofing”) so that the timestep will be limited by the longer advective timescale. The anelastic approximation does this by replacing the full continuity equation with the kinematic constraint that the mass flux be divergence-free. This approximation still allows for the effects of density stratification (e.g., buoyancy in the vertical momentum equation, pressure–volume work in the energy/entropy equation) and has been employed extensively in the study of deep, subsonic convection in planetary atmospheres [4,24,37] and stars [20,34]. In [8], we re-derived the anelastic approximation in the context of protoplanetary disks. Stratified media support the propagation of internal gravity waves. As these waves travel from high density to low density regions, their amplitudes can grow to large values (so as to conserve energy flux). If the density contrast is large, velocity and thermodynamic fluctuations can become sufficiently large so as to invalidate the anelastic approximation and/or violate the CFL condition. We have developed a technique based on “negative feedback” to damp these waves when they propagate into low-density gas which has very little inertia.

We compute the evolution of the anelastic equations with a spectral method. The basic philosophy of spectral methods is to approximate any function of interest with a finite sum of basis functions multiplied by spectral coefficients [11,13,23,30]. A partial differential equation (PDE) in space and time is reduced to a coupled set of ordinary differential equations (ODE) for the time evolution of the spectral coefficients. The chief advantage of spectral methods over finite-difference methods is accuracy per degrees of freedom (e.g., number of spectral modes or number of grid points). In one dimension, the global error (e.g., L_2 norm) for a finite-difference method with N grid points scales as $(1/N)^p$, where p is the (fixed) order of the method, whereas for a spectral method with N spectral modes, the error scales as $(1/N)^N$. Thus, to get the same level of accuracy, spectral methods generally require far fewer degrees of freedom. This advantage is even more pronounced in 3D problems requiring high resolution.

Because of the linear background shear, the fluid equations depend explicitly on the cross-stream coordinate (i.e., non-autonomous), making it problematic to apply periodic boundary conditions in this direction. The equations can be made autonomous in the horizontal directions by transforming to a set of Lagrangian shearing coordinates [22,33,39]. Features in the flow that are advected by the shear appear quasi-stationary in the shearing coordinates, allowing for larger timesteps to be taken in the numerical integration. Because the background state generally depends on the vertical coordinate, we do not impose periodicity in the vertical direction. We have implemented the code with two different sets of vertical basis functions: (1) Chebyshev polynomials on a truncated, finite domain, and (2) rational Chebyshev functions on an infinite domain. Use of this latter set is equivalent to transforming the infinite domain to a finite one with a cotangent mapping, and using cosine and sine expansions in the mapped coordinate [11,12].

The code is pseudospectral. That is, nonlinear terms are not computed via convolution, which is computationally slow; rather, they are computed on a grid of collocation points, and then transformed to wavenumber space with fast Fourier transforms (FFTs). Different horizontal Fourier modes interact only through these nonlinear terms and are otherwise independent. This motivated us to divide the domain into blocks along the two horizontal directions, but not along the vertical direction. That is, on a parallel machine, each processor works with only a subset of the horizontal Fourier wavenumbers, but with all of the vertical data corresponding to those horizontal wavenumbers. The reason we do not split the vertical direction across different processors is that the Poisson-like equation for the pressure/enthalpy couples all of the vertical Chebyshev modes, especially if the stratification is a complicated function of height. Because this direction is not split, inverting the Poisson-like equation involves no cross-processor communication. The only time in the simulation that different processors communicate with one another is in the computation of the FFTs needed for the nonlinear terms. In general, spectral methods require more cross-processor communication than finite-difference methods, but this is roughly balanced by the fact that less degrees of freedom are needed to achieve the same level of accuracy. The results of our timing tests indicate that we get excellent parallel performance with the message passing interface (MPI) on the IBM Blue Horizon (now decommissioned) and Datastar supercomputers at the San Diego Supercomputer Center.

In some applications (e.g., protoplanetary disks), magnetic fields may play an important role in the development of turbulence via the magnetorotational instability [2,3,14,44]. However, it is still not yet clear whether protoplanetary disks are sufficiently ionized to couple the gas to the magnetic fields [9], except perhaps in thin surface layers that are ionized by protostellar X-rays and cosmic rays [19]. For now, in this work, we will neglect the effects of magnetic fields. However, they will be added to a future version of the code, and we will explore their effects on the dynamics.

We note that there are currently several publicly-available, finite-difference codes that solve the equations of compressible magnetohydrodynamics (MHD), including ZEUS [41–43] and ATHENA [40], the latter of which uses a higher-order Godunov method. The motivation for developing a new code based on spectral methods is to take advantage of the higher accuracy and resolution so that one can more effectively study structures on the smallest scales that would otherwise be smeared out by numerical or grid viscosity. Comparisons with these finite-difference MHD codes will be made in future work. One of the most widely used codes for computing flows in the atmospheres of giant planets is the explicit planetary isentropic-coordinate (EPIC) atmospheric model code [17]. This is also a finite-difference code, but one that employs isentropic coordinates, and therefore is unable to compute overturning and vertical mixing that might make the vertical entropy profile non-monotonic. Another popular algorithm for atmospheric flows is the contour-advective semi-Lagrangian (CASL) method [16,18,28,35], in which the boundaries of piecewise regions of constant potential vorticity (which is advectively conserved in the quasi-geostrophic limit) are tracked. This method, however, would not be appropriate to compute the flow in a protoplanetary disk because the gas is unstratified in the midplane, making it difficult to identify a useful form of the potential vorticity.

In this paper, we focus on the development of the algorithms to solve the anelastic equations in rotating and shearing systems. In Section 2, we will review the anelastic equations with shear. In Section 3, we will describe the spectral method in detail. In Section 4, we will present tests of accuracy and performance, and preview potential applications. Finally, in Section 5, we will outline future work on these applications, as well as propose further improvements to these simulations (including the addition of magnetic fields). In future works, we will apply the code to the flow in protoplanetary disks [7] and planetary atmospheres, and make detailed comparisons with the previous results of other codes.

2. Anelastic equations with shear

For clarity, we define up-front the following flow variables (vectors are represented with bold type): velocity \mathbf{v} , vorticity $\boldsymbol{\omega} \equiv \nabla \times \mathbf{v}$, pressure p , density ρ , temperature T , entropy s , and potential temperature θ . For an ideal gas: $p = \rho \mathcal{R} T$ and $s = C_v \ln(p \rho^{-\gamma}) + s_0 = C_p \ln \theta + s'_0$, where C_v is the specific heat at constant volume, C_p is the specific heat at constant pressure, $\mathcal{R} \equiv C_p - C_v$ is the gas constant, $\gamma \equiv C_p / C_v$ is the ratio of specific heats, and s_0, s'_0 are integration constants. We work in a Cartesian coordinate system

(x, y, z) with corresponding unit vectors $(\hat{\mathbf{x}}, \hat{\mathbf{y}}, \hat{\mathbf{z}})$. The rotation axis is aligned with the $+z$ axis: $\boldsymbol{\omega} = \Omega \hat{\mathbf{z}}$, and the acceleration of gravity points in the negative z direction: $\mathbf{a}_{\text{grav}} = -g \hat{\mathbf{z}}$.

Each flow variable is represented as the sum of a time-independent background component, denoted with overbars, and a time-varying component, denoted with tildes (e.g., $\mathbf{v} = \bar{\mathbf{v}} + \tilde{\mathbf{v}}$). The background velocity field is a unidirectional shear flow that is parallel to the x -axis and varies only with the y coordinate (see Fig. 1):

$$\bar{\mathbf{v}} = -\sigma y \hat{\mathbf{x}}, \quad (1)$$

where σ is the constant shear rate. The background vorticity corresponding to this shear flow is $\bar{\boldsymbol{\omega}} = \sigma \hat{\mathbf{z}}$. The shear is cyclonic if σ and Ω have the same sign, and anticyclonic if they have opposite signs. The background thermodynamic state, which we assume depends only on the vertical coordinate z , is in hydrostatic balance:

$$\frac{d\bar{p}}{dz} = -\bar{\rho}g. \quad (2)$$

An important measure of the stratification is the Brunt–Väisälä frequency, or the frequency of buoyancy-driven oscillations in a convectively stable atmosphere:

$$\omega_B^2(z) \equiv \frac{g}{C_p} \frac{d\bar{s}}{dz} \equiv \frac{g}{\bar{\theta}} \frac{d\bar{\theta}}{dz}. \quad (3)$$

There are many different variations of the anelastic approximation [4,20,24,37]. The key assumption they all share is that the flow is subsonic and the thermodynamic fluctuations are small relative to their background values:

$$\epsilon^2 \equiv \left(\frac{\tilde{v}}{c_s}\right)^2 \sim \frac{\tilde{p}}{\bar{p}} \sim \frac{\tilde{\rho}}{\bar{\rho}} \sim \frac{\tilde{T}}{\bar{T}} \sim \frac{\tilde{\theta}}{\bar{\theta}} \ll 1, \quad (4)$$

where ϵ is the Mach number and c_s is the local sound speed. In a typical derivation, all variables are expressed as asymptotic series expansions in powers of the Mach number ϵ , the expansions are substituted into the governing fluid equations, and terms are grouped by like powers of ϵ . In [8], we derived a version of the anelastic approximation for a protoplanetary disk with a constant temperature background. Here, we present a more general version proposed by Bannon [4], but modified to include a background shear:

$$0 = \frac{1}{\bar{\rho}} \nabla \cdot \bar{\rho} \tilde{\mathbf{v}} = \nabla \cdot \tilde{\mathbf{v}} + \left(\frac{d \ln \bar{\rho}}{dz}\right) \tilde{v}_z, \quad (5a)$$

$$\left(\frac{\partial}{\partial t} - \sigma y \frac{\partial}{\partial x}\right) \tilde{\mathbf{v}} = \sigma \tilde{v}_y \hat{\mathbf{x}} + \tilde{\mathbf{v}} \times (\bar{\boldsymbol{\omega}} + 2\Omega \hat{\mathbf{z}}) - \nabla \tilde{h} + \frac{\tilde{\theta}}{\bar{\theta}} g \hat{\mathbf{z}}, \quad (5b)$$

$$\left(\frac{\partial}{\partial t} - \sigma y \frac{\partial}{\partial x}\right) \tilde{\theta} = -\tilde{\mathbf{v}} \cdot \nabla \tilde{\theta} - \frac{d\tilde{\theta}}{dz} \tilde{v}_z, \quad (5c)$$

$$\tilde{h} = \tilde{p}/\bar{\rho} + \tilde{v}^2/2, \quad (5d)$$

$$\tilde{p}/\bar{p} = \tilde{\rho}/\bar{\rho} + \tilde{T}/\bar{T}, \quad (5e)$$

$$\tilde{\theta}/\bar{\theta} = \tilde{p}/(\bar{\rho}gH_p) - \tilde{\rho}/\bar{\rho}, \quad (5f)$$

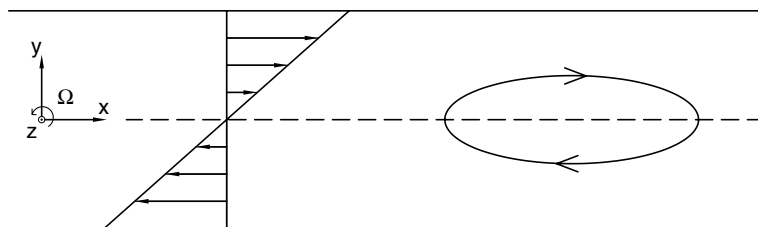


Fig. 1. Horizontal linear shear flow: $\bar{\mathbf{v}} = -\sigma y \hat{\mathbf{x}}$. The system rotates counterclockwise around the $+z$ -axis (which points out of the page) at a rate Ω . The horizontal shear and vortex illustrated in this example are anticyclonic: $\sigma < 0$. Gravity points in the $-z$ direction (into the page).

where we have defined a dynamic enthalpy \tilde{h} , and a density scale height $H_\rho \equiv |(\text{d ln } \bar{\rho} / \text{d}z)^{-1}|$. The error in the anelastic approximation due to the neglected terms scales as $\mathcal{O}(\epsilon^2)$. The careful reader may note that Eq. (5f) is not the “correct” linearization of the potential temperature; the denominator in the pressure term should be $\gamma\bar{p}$. Bannon [4] shows that, in the absence of dissipation and heat sources/sinks, the anelastic equations do not conserve energy unless one makes the replacement $\gamma\bar{p} \rightarrow \bar{\rho}gH_\rho$.

In the case where the background is constant temperature $\bar{T} = T_0$, we can eliminate the potential temperature in favor of the gas temperature via [4,8]:

$$\frac{\tilde{\theta}}{\bar{\theta}} \rightarrow \frac{\tilde{T}}{T_0}, \tag{6a}$$

$$\left(\frac{\partial}{\partial t} - \sigma y \frac{\partial}{\partial x}\right)\tilde{T} = -\tilde{\mathbf{v}} \cdot \nabla \tilde{T} - \frac{\omega_{\mathbf{B}}^2}{g}(T_0 + \tilde{T})\tilde{v}_z. \tag{6b}$$

Again, we note that (6a) follows from (5f), not from a direct linearization of the potential temperature.

It is useful for diagnostic purposes to identify energy-like conserved quantities for the anelastic system (5a). We define kinetic, shear, and thermal energies:

$$E_K \equiv \int_V \bar{\rho} \tilde{v}^2 / 2 \, \text{d}V, \tag{7a}$$

$$E_S \equiv \int_V \bar{\rho} \tilde{v}_x \tilde{v}_x \, \text{d}V, \tag{7b}$$

$$E_T \equiv \int_V C_p \bar{\rho} \tilde{T} (\tilde{\theta} / \bar{\theta}) \, \text{d}V, \tag{7c}$$

where we integrate over the computational volume V : $-L_x/2 \leq x \leq L_x/2$, $-L_y/2 \leq y \leq L_y/2$, and $-L_z \leq z \leq L_z$. For this exercise, we assume that all quantities with a tilde are periodic in x and y .² We also assume that if L_z is finite, then $\tilde{v}_z = 0$ at $z = \pm L_z$, or if $L_z \rightarrow \infty$, then $\tilde{v}_z \rightarrow 0$. To obtain an equation for the evolution of the kinetic energy, take the dot product of the momentum flux $\bar{\rho} \tilde{\mathbf{v}}$ with the momentum equation (5b) and integrate over the domain V . Many of the resulting terms can be written as perfect divergences which will integrate to zero with periodicity in x and y and the vertical boundary conditions. The terms that survive the integration are source/sink terms for the kinetic energy. For the evolution of the shear energy, multiply the x -component of the momentum equation (5b) by $\bar{\rho} \tilde{v}_x$, and integrate over V . Here, the integration is not so simple because y times a tilde quantity is not necessarily periodic in y ; this will lead to surface terms that do not cancel. For the evolution of the thermal energy, multiply the potential temperature equation (5c) by $C_p \bar{\rho} \tilde{T} / \bar{\theta}$ and integrate over V . The resulting energy evolution equations are:

$$\text{d}E_K / \text{d}t = +\mathcal{E}_1 + \mathcal{E}_2, \tag{8a}$$

$$\text{d}E_S / \text{d}t = -\mathcal{E}_1 + \mathcal{E}_3, \tag{8b}$$

$$\text{d}E_T / \text{d}t = -\mathcal{E}_2, \tag{8c}$$

$$\text{d}(E_K + E_S + E_T) / \text{d}t = +\mathcal{E}_3, \tag{8d}$$

where the energy source/sink terms are defined:

$$\mathcal{E}_1 \equiv \int_V \sigma \bar{\rho} \tilde{v}_x \tilde{v}_y \, \text{d}V, \tag{9a}$$

$$\mathcal{E}_2 \equiv \int_V \bar{\rho} (\tilde{\theta} / \bar{\theta}) g \tilde{v}_z \, \text{d}V, \tag{9b}$$

$$\mathcal{E}_3 \equiv \int_{y=L_y/2} \sigma \bar{\rho} \tilde{v}_x \tilde{v}_y L_y \, \text{d}x \, \text{d}z. \tag{9c}$$

² We have not yet introduced the shearing coordinates, but if one did this exercise assuming that variables with tildes are periodic in the shearing coordinates, one would get the exact same result.

There are two source/sink terms for the kinetic energy: exchange with the background shear, and exchange with the thermal energy. As expected, these same terms appear, with opposite signs, in the evolution equations for the shear and thermal energies. We can define a “total” energy which is the sum of kinetic, shear, and thermal energies. The evolution equation for the total energy has only one source/sink term, which is the surface term from the shear energy evolution equation. This term represents the flow of energy into and out of the edges of the domain in the cross-stream direction.

3. Spectral method

Let $q(x, y, z, t)$ represent some arbitrary variable, which may be either a scalar or a component of a vector field. We write:

$$q(x, y, z, t) \approx \sum_{\ell=-\frac{N_x}{2}+1}^{\frac{N_x}{2}} \sum_{m=-\frac{N_y}{2}+1}^{\frac{N_y}{2}} \sum_{n=0}^{N_z} \hat{q}_{\ell mn}(t) e^{ik_x x} e^{ik_y y} \phi_n(z), \quad (10)$$

where ℓ, m, n are integers, and $\{\hat{q}_{\ell mn}(t)\}$ are the set of spectral coefficients. The Fourier–Fourier basis in x and y has wavenumbers: $\{k_x \equiv \ell \Delta k_x, k_y \equiv m \Delta k_y\}$, where $\Delta k_x \equiv 2\pi/L_x$, $\Delta k_y \equiv 2\pi/L_y$, and where L_x and L_y are the dimensions of the periodic box. The basis functions for the vertical direction, $\phi_n(z)$, will be defined in Section 3.2. If q is a real function (and if the $\phi_n(z)$ are real functions of z), then we have the reality condition: $\hat{q}_{\ell mn}^* = \hat{q}_{-\ell, -m, n}$, where $(\)^*$ represents complex conjugation. We only need to keep track of half the spectral coefficients, say, for $\ell \geq 0$.

Our approach is a pseudospectral method. Products of two or more variables are *not* computed via convolution, which is computationally expensive. Instead, we define a grid of collocation points: $\{x_\ell \equiv \ell \Delta x, y_m \equiv m \Delta y, z_n\}$, where $\Delta x \equiv L_x/N_x$ and $\Delta y \equiv L_y/N_y$. The collocation points are uniformly spaced in x and y , but not in z (see Section 3.2). A variable can equally be represented by its set of spectral coefficients $\{\hat{q}_{\ell mn}\}$ (“wave-number space” or “FFF-space”) or by the values of the variable at the set of grid points $\{q(x_\ell, y_m, z_n)\}$ (“physical space” or “PPP-space”). We go between these two representations with the use of fast Fourier transforms (FFTs):

$$\{\hat{q}_{\ell mn}\} \xleftrightarrow{\text{FFT}} \{q(x_\ell, y_m, z_n)\}. \quad (11)$$

To compute a product of two or more variables, we transform each variable to physical space, multiply the variables at each collocation point, and then transform the product back to wavenumber space. The product will be contaminated with aliasing errors, but these will be small if the variables are well-resolved (that is, the spectral coefficients for high wavenumbers are sufficiently small). Finally, we mention that at times we will work in “mixed” space in which the horizontal directions are in Fourier–Fourier space, but the vertical direction is untransformed: $\{\hat{q}_{\ell m}(z_n)\}$. We call this “FFP-space”.

3.1. Shearing coordinates

The anelastic equations with shear (5a) are autonomous in time t and the streamwise direction x , but are non-autonomous in the cross-stream direction y and the vertical direction z . It would be ideal if we could make the equations autonomous in y before imposing periodicity. Fortunately, this can be done by transforming to a set of quasi-Lagrangian coordinates that advect with the background shear [22,33,39]:

$$t' \equiv t, \quad (12a)$$

$$x' \equiv x + \sigma y t, \quad (12b)$$

$$y' \equiv y, \quad (12c)$$

$$z' \equiv z. \quad (12d)$$

The Jacobian for this coordinate transformation is unity; the volume of a computational cell is preserved as it is sheared. Partial derivatives in the two coordinate systems are related via the chain rule:

$$\frac{\partial}{\partial t} = \frac{\partial}{\partial t'} + \sigma y' \frac{\partial}{\partial x'}, \tag{13a}$$

$$\frac{\partial}{\partial x} = \frac{\partial}{\partial x'}, \tag{13b}$$

$$\frac{\partial}{\partial y} = \frac{\partial}{\partial y'} + \sigma t' \frac{\partial}{\partial x'}, \tag{13c}$$

$$\frac{\partial}{\partial z} = \frac{\partial}{\partial z'}, \tag{13d}$$

$$\nabla = \nabla' + \hat{y} \sigma t' \frac{\partial}{\partial x'}. \tag{13e}$$

The anelastic equations in the the shearing coordinates are:

$$0 = \left[\left(\nabla' + \hat{y} \sigma t' \frac{\partial}{\partial x'} \right) + \hat{z} \left(\frac{d \ln \bar{\rho}}{dz} \right) \right] \cdot \tilde{\mathbf{v}}, \tag{14a}$$

$$\frac{\partial \tilde{\mathbf{v}}}{\partial t'} = \sigma \tilde{v}_y \hat{\mathbf{x}} + \tilde{\mathbf{v}} \times (\tilde{\boldsymbol{\omega}} + 2\Omega \hat{\mathbf{z}}) - \left(\nabla' + \hat{y} \sigma t' \frac{\partial}{\partial x'} \right) \tilde{h} + \frac{\tilde{\theta}}{\theta} g \hat{\mathbf{z}}, \tag{14b}$$

$$\frac{\partial \tilde{\theta}}{\partial t'} = -\tilde{\mathbf{v}} \cdot \left(\nabla' + \hat{y} \sigma t' \frac{\partial}{\partial x'} \right) \tilde{\theta} - \frac{d\tilde{\theta}}{dz} \tilde{v}_z, \tag{14c}$$

where the vorticity is now: $\tilde{\boldsymbol{\omega}} \equiv (\nabla' + \hat{y} \sigma t' \partial/\partial x') \times \tilde{\mathbf{v}}$. The equations are autonomous in both x' and y' , at the expense that the equations explicitly depend on time t' .

Variables are represented by Fourier–Fourier expansions in the shearing coordinates, not in the original coordinates. From the point of view of the original coordinates, the computational grid is sheared with the background flow (see Fig. 2). If left unchecked, the computational grid will become greatly distorted in time: lines of constant x' will approach being parallel with lines of constant y' . Periodically, it will be necessary to re-map the shearing coordinate system back onto a rectangular Cartesian grid [39]. This should not be done at any arbitrary time. In general, variables will not be periodic with respect to the original

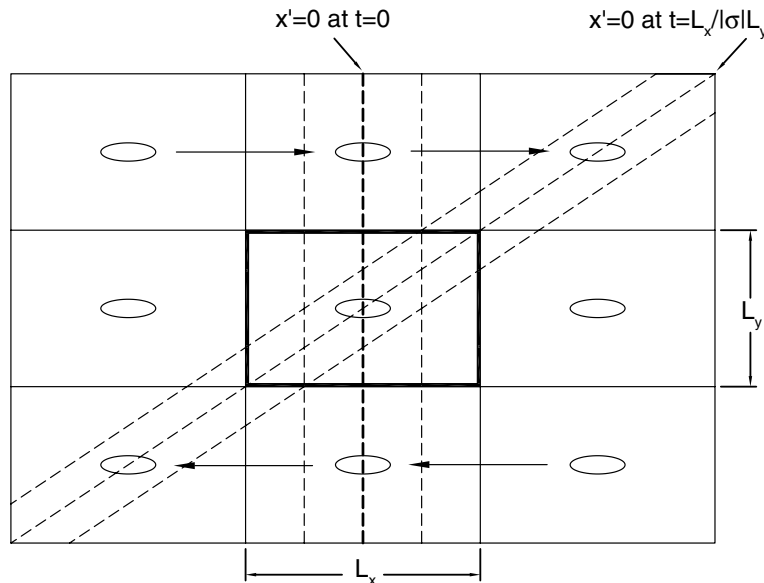


Fig. 2. Lagrangian shearing coordinates that advect with the shear. In this example, $\sigma < 0$. Center box is computational domain of size (L_x, L_y) . Eight periodic images are also shown. The dashed vertical lines correspond to lines of constant x' at time $t=0$. At time $t = t_{rm} \equiv L_x/|\sigma|L_y$, the periodic images, which are carried with the shearing coordinates, have realigned – this is the optimal time to re-map the sheared coordinates back onto a Cartesian grid.

coordinates except at those special times when the periodic images line up again vertically. We define this to be the re-map time:

$$t_{\text{rm}} \equiv \frac{L_x}{|\sigma|L_y}. \quad (15)$$

In physical space, the coordinates of a computational cell after re-mapping $(x_{\text{rm}}, y_{\text{rm}})$ can be found by inverting (12a) and evaluating at the re-map time:

$$x_{\text{rm}} = x' - \sigma y' t_{\text{rm}} = x' \mp \frac{L_x}{L_y} y', \quad (16a)$$

$$y_{\text{rm}} = y', \quad (16b)$$

where the upper sign corresponds to $\sigma > 0$ and the lower sign corresponds to $\sigma < 0$. Using the well-known Fourier shift theorem, the re-map process can also be done in FPP-space (x direction is in Fourier space, but the y and z directions in physical space):

$$\hat{q}_\ell^{\text{rm}}(y, z, t_{\text{rm}}) = \hat{q}_\ell(y', z', t_{\text{rm}}) \exp(ik_x \sigma y t_{\text{rm}}) = \hat{q}_\ell(y', z', t_{\text{rm}}) \exp(\pm 2\pi i \ell y / L_y), \quad (17)$$

where the top sign corresponds to $\sigma > 0$, and the bottom sign corresponds to $\sigma < 0$.

We re-map the three components of velocity and the potential temperature, but not the dynamic enthalpy. In an anelastic code, the enthalpy is not a dynamic variable; rather, it adjusts instantaneously to maintain the divergence-free condition on the momentum. The enthalpy should be recomputed from the Poisson-like equation after the momentum and potential temperature have been re-mapped (see Section 3.3).

3.2. Vertical basis functions

In general, the background state may depend explicitly on the vertical coordinate z . Rather than imposing artificial periodicity in the vertical direction, we employ two different domain mapping methods [11,13]. The first mapping that we use is a cosine mapping:

$$z = L_z \cos \xi, \quad 0 \leq \xi \leq \pi, \quad (18)$$

which truncates the vertical domain to be within $|z| \leq L_z$. When we couple this mapping with a cosine series expansion, the resulting basis functions are the Chebyshev polynomials:

$$T_n\left(\frac{z}{L_z}\right) \equiv \cos(n\xi) \equiv \cos\left(n \cos^{-1} \frac{z}{L_z}\right). \quad (19)$$

That is, use of a cosine basis in the mapped coordinate ξ is completely equivalent to using a Chebyshev basis in the original coordinate z . One disadvantage of this approach is that the collocation points (which are uniformly spaced in the mapped coordinate ξ) are clustered near the boundaries $z = \pm L_z$ (see Fig. 3). This can be ameliorated via another transformation that makes the spacing more even [26]. Another disadvantage is the need to impose what may be unphysical boundary conditions at the boundaries $z = \pm L_z$. Although there are ways of formulating non-reflecting boundary conditions for simple problems [21], the horizontal shear,

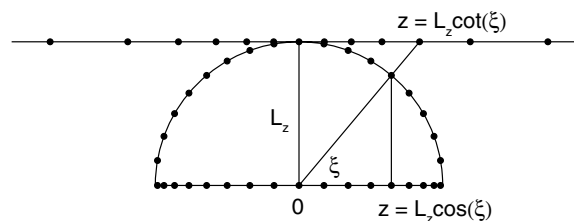


Fig. 3. Cosine mapping versus cotangent mapping. The coordinate ξ is uniformly spaced around the semi-circle from 0 to π . The cosine mapping clusters collocation points near the boundaries, whereas the cotangent mapping concentrates collocation points around center of the domain.

vertical stratification, and nonlinearities associated with advective terms make this problematic. In Section 3.3.2, we describe a method to damp gravity waves near the artificial boundaries.

The problems associated with the clustering of grid points at the artificial boundaries as well the imposition of artificial boundary conditions can be solved with a mapping that puts the boundaries off to infinity. To do this, we use a cotangent mapping [11,12]:

$$z = L_z \cot \xi, \quad 0 \leq \xi \leq \pi, \tag{20}$$

which allows us to treat the entire infinite domain $-\infty < z < \infty$. With this mapping, half of the collocation points are within $|z| \leq L_z$, and they are more clustered around $z = 0$ (see Fig. 3). The other half of the collocation points are widely spaced beyond $|z| > L_z$. We couple this mapping with both cosine and sine series:

$$C_n\left(\frac{z}{L_z}\right) \equiv \cos(n\xi) \equiv \cos\left(n \cot^{-1} \frac{z}{L_z}\right), \tag{21a}$$

$$S_n\left(\frac{z}{L_z}\right) \equiv \sin(n\xi) \equiv \sin\left(n \cot^{-1} \frac{z}{L_z}\right). \tag{21b}$$

Boyd [11] calls these functions “rational Chebyshev functions” (although only the functions for even n are rational, whereas the ones for odd n are irrational functions).

Why do we couple the cotangent mapping with *both* cosine and sine expansions, whereas with the cosine mapping, we use only cosine expansions? The derivative of the n th Chebyshev polynomial is (with $L_z = 1$):

$$\frac{dT_n(z)}{dz} = \frac{n \sin(n\xi)}{\sin(\xi)} = 2n \sum_{\substack{j=0 \\ j+n \text{ odd}}}^{n-1} \alpha_j \cos(j\xi) = 2n \sum_{\substack{j=0 \\ j+n \text{ odd}}}^{n-1} \alpha_j T_j(z), \tag{22}$$

where $\alpha_0 = 1/2$ and $\alpha_j = 1$ for $j > 0$. That is, the derivative of a Chebyshev polynomial is just a finite series of lower degree Chebyshev polynomials of opposite parity.

On the other hand, the derivatives of the rational Chebyshev functions are (with $L_z = 1$):

$$\begin{aligned} \frac{dC_n(z)}{dz} &= n \sin(n\xi) \sin^2(\xi) = n\{-\sin[(n-2)\xi] + 2\sin(n\xi) - \sin[(n+2)\xi]\} \\ &= n[-S_{n-2}(z) + 2S_n(z) - S_{n+2}(z)], \end{aligned} \tag{23a}$$

$$\begin{aligned} \frac{dS_n(z)}{dz} &= -n \cos(n\xi) \sin^2(\xi) = -n\{-\cos[(n-2)\xi] + 2\cos(n\xi) - \cos[(n+2)\xi]\} \\ &= -n[-C_{n-2}(z) + 2C_n(z) - C_{n+2}(z)]. \end{aligned} \tag{23b}$$

The derivative of a rational Chebyshev function of the cosine kind is a three-term sum of rational Chebyshev functions of the sine kind, and vice versa. In principle, one could represent the derivative of $C_n(z)$ with a convergent infinite series of $C_n(z)$, obviating the need for $S_n(z)$. However, we prefer to work with recursion relations with finite numbers of terms, such as (23). Other recursion relations for the rational Chebyshev functions can be found in Appendix C.

Boyd [11] has an extensive discussion on the asymptotic behavior of the rational Chebyshev functions. We want to point out that the choice of cosine or sine kind in representing a given function is *not* determined by the parity of the function (i.e., whether it is an even or odd function), but on the asymptotic behavior of the function at infinity. The rational Chebyshev functions of the cosine kind approach their asymptotic values in even powers of $1/y$, whereas those of the sine kind approach their asymptotic values in odd powers of $1/y$.

The product of two variables represented by the same kind of rational Chebyshev functions results in a series of the cosine kind, whereas the product of two variables represented by different kinds of rational Chebyshev functions results in a series of the sine kind. Multiplying a variable by a function that is odd with respect to z causes its series expansion to switch kinds. Every term in a given equation should be represented by the same kind of expansion. Thus, when we use the rational Chebyshev functions for the vertical basis functions, \tilde{v}_x , \tilde{v}_y , $\tilde{\omega}_z$, $\tilde{\theta}$, and \tilde{h} are represented with rational Chebyshev functions of the cosine kind, whereas \tilde{v}_z , $\tilde{\omega}_x$, and $\tilde{\omega}_y$ are represented with rational Chebyshev functions of the sine kind.

3.3. Time integration algorithms

In this section, we describe algorithms for integrating the anelastic equations forward in time. Let the hat symbol (e.g., \hat{q}) denote a variable whose horizontal directions are in Fourier space (for clarity, we drop the subscripts ℓ, m previously introduced). One may think of \hat{q} as either a column vector of the values of the variable at the different vertical positions (i.e., FFP-space), or a column vector of vertical spectral coefficients (i.e., FFF-space); which of these is intended will be clear from the context.

The equations are integrated in time via the method of “fractional steps”. The velocity is integrated in four steps: an advection step, a hyperviscosity step, an explicit pressure step, and an implicit pressure step. The potential temperature is integrated in two steps: an advection step and a hyperdiffusion step. We use a superscript N to denote a variable at the N th timestep (e.g., $t^N \equiv N\Delta t$, $\hat{\mathbf{v}}^N \equiv \hat{\mathbf{v}}(t = t^N)$). A fraction in the superscript denotes a variable at an intermediate stage of the integration, not after some fraction of a timestep (e.g., $\hat{\mathbf{v}}^{N+1/4}$ is the velocity after the first of four intermediate steps). We have not employed any adaptive timestep algorithms; the timestep is a constant in all our simulations.

We have implemented two versions of the advection step, both based on an explicit second-order Adams–Bashforth method. In one method, the nonlinear advection terms are treated explicitly and the linear terms (Coriolis and buoyancy) are treated semi-analytically. In the other method, the advection, Coriolis, and buoyancy terms are all treated explicitly, but with additional terms that damp internal gravity waves in low-density regions. For the pressure step, we use the semi-implicit second-order Crank–Nicholson method. We have confirmed that there are no low order splitting errors, so that the algorithms are globally second-order accurate in time.

3.3.1. Step 1: Advection — semi-analytic treatment of Coriolis and buoyancy forces

The Coriolis force couples the horizontal components of the velocity, resulting in inertial oscillations with the Coriolis frequency (modified by linear shear): $\omega_C \equiv \sqrt{2\Omega(2\Omega + \sigma)}$. Similarly, buoyancy and pressure–volume work couple the vertical velocity and the potential temperature, resulting in buoyant oscillations (e.g., internal gravity waves) with the Brunt–Väisälä frequency ω_B [27,38]. Both inertial and buoyant oscillations can be described by the simple set of coupled ordinary differential equations:

$$\dot{u}_1 = +\alpha_1 u_2 + f_1, \quad (24a)$$

$$\dot{u}_2 = -\alpha_2 u_1 + f_2, \quad (24b)$$

where a dot denotes time differentiation, $\alpha_1 > 0$, $\alpha_2 > 0$, and f_1, f_2 are forcing constants. The exact solution for arbitrary time t is:

$$u_1(t) = u_1(0) \cos(\omega t) + u_2(0) \left(\frac{\alpha_1}{\omega}\right) \sin(\omega t) + f_1 t \left[\frac{\sin(\omega t)}{\omega t}\right] + f_2 \left(\frac{\alpha_1 t^2}{2}\right) \left[\frac{2(1 - \cos(\omega t))}{(\omega t)^2}\right], \quad (25a)$$

$$u_2(t) = u_2(0) \cos(\omega t) - u_1(0) \left(\frac{\alpha_2}{\omega}\right) \sin(\omega t) + f_2 t \left[\frac{\sin(\omega t)}{\omega t}\right] - f_1 \left(\frac{\alpha_2 t^2}{2}\right) \left[\frac{2(1 - \cos(\omega t))}{(\omega t)^2}\right], \quad (25b)$$

where we have defined $\omega^2 \equiv \alpha_1 \alpha_2$.

We use the above solution as a template for a new integration scheme in which the forcing terms (e.g., f_1, f_2) are not constants in time, but correspond to nonlinear advection terms, which we treat with an Adams–Bashforth scheme:

$$\hat{\mathfrak{R}} \equiv \frac{3}{2} \left[(\hat{\mathbf{v}} \times \hat{\omega})^N \right] - \frac{1}{2} \left[(\hat{\mathbf{v}} \times \hat{\omega})^{N-1} \right], \quad (26a)$$

$$\hat{\mathfrak{M}} \equiv \frac{3}{2} \left[-(\hat{\mathbf{v}} \cdot \nabla \hat{\theta})^N \right] - \frac{1}{2} \left[-(\hat{\mathbf{v}} \cdot \nabla \hat{\theta})^{N-1} \right]. \quad (26b)$$

The velocity and potential temperature are updated via:

$$\hat{v}_x^{N+\frac{1}{4}} = \cos(\omega_C \Delta t) \hat{v}_x^N + \Delta t q_1(\omega_C \Delta t) [(2\Omega + \sigma) \hat{v}_y^N + \hat{\mathfrak{R}}_x] + \frac{1}{2} \Delta t^2 q_2(\omega_C \Delta t) (2\Omega + \sigma) [\hat{\mathfrak{R}}_y - i(k'_y + \sigma t k'_x) \hat{h}^N], \quad (27a)$$

$$\hat{v}_y^{N+\frac{1}{4}} = \cos(\omega_C \Delta t) \hat{v}_y^N + \Delta t q_1(\omega_C \Delta t) [(-2\Omega) \hat{v}_x^N + \hat{\mathfrak{R}}_y] + \frac{1}{2} \Delta t^2 q_2(\omega_C \Delta t) (-2\Omega) [\hat{\mathfrak{R}}_x - i k'_x \hat{h}^N], \quad (27b)$$

$$\hat{v}_z^{N+\frac{1}{4}} = \cos(\omega_B \Delta t) \hat{v}_z^N + \Delta t q_1(\omega_B \Delta t) [(g/\bar{\theta}) \hat{\theta}^N + \hat{\mathfrak{R}}_z] + \frac{1}{2} \Delta t^2 q_2(\omega_B \Delta t) (g/\bar{\theta}) [\hat{\mathfrak{R}}_z], \quad (27c)$$

$$\hat{\theta}^{N+\frac{1}{2}} = \cos(\omega_B \Delta t) \hat{\theta}^N + \Delta t q_1(\omega_B \Delta t) [(-d\bar{\theta}/dz) \hat{v}_z^N + \hat{\mathfrak{M}}] + \frac{1}{2} \Delta t^2 q_2(\omega_B \Delta t) (-d\bar{\theta}/dz) [\hat{\mathfrak{R}}_z - \partial \hat{h}^N / \partial z], \quad (27d)$$

where the functions q_1 and q_2 are defined as:

$$q_1(\tau) = \sin(\tau)/\tau, \quad (28a)$$

$$q_2(\tau) = 2[1 - \cos(\tau)]/\tau^2. \quad (28b)$$

The time differencing error for one step scales as Δt^3 . For $\omega_{C/B} \Delta t \ll 1$, q_1 and q_2 can be replaced with unity without changing how the error scales with the size of the step.

3.3.2. Step 1: Advection – explicit treatment of Coriolis and buoyancy forces with gravity-wave damping

As an internal gravity wave propagates from a high density region into a low density region, its amplitude increases so as to conserve energy flux. If the density contrast is large, velocity and thermodynamic fluctuations can become sufficiently large so as to invalidate the anelastic approximation and/or violate the CFL condition. We have developed a strategy to control gravity waves that is akin to “negative feedback” in circuit theory. Mathematically, the origin of the buoyant oscillations is the fact that the time derivative of the vertical velocity depends linearly on the potential temperature, and vice versa. Physically, a hot parcel of fluid rises into less dense material, expands and cools; it then sinks, compresses, and heats-up, and the cycle continues. To damp these oscillations, we add a term proportional to the *time derivative* of the potential temperature to the vertical velocity equation, and vice versa. This introduces a term that is proportional to $-\bar{v}_z$ into the equation for the vertical velocity, and a term that is proportional to $-\bar{\theta}$ into the equation for the potential temperature. In the following integration scheme, we add the Coriolis and buoyancy terms to the nonlinear advection terms and treat them all with an Adams–Bashforth scheme:

$$\hat{\mathfrak{R}} \equiv \frac{3}{2} \left[(\widehat{\bar{\mathbf{v}} \times \bar{\omega}})^N - 2\Omega \hat{\mathbf{z}} \times \hat{v}^N + \sigma \hat{v}_y^N \hat{\mathbf{x}} + \frac{\hat{\theta}^N}{\bar{\theta}} g \hat{\mathbf{z}} \right] - \frac{1}{2} \left[(\widehat{\bar{\mathbf{v}} \times \bar{\omega}})^{N-1} - 2\Omega \hat{\mathbf{z}} \times \hat{v}^{N-1} + \sigma \hat{v}_y^{N-1} \hat{\mathbf{x}} + \frac{\hat{\theta}^{N-1}}{\bar{\theta}} g \hat{\mathbf{z}} \right], \quad (29a)$$

$$\hat{\mathfrak{M}} \equiv \frac{3}{2} \left[-(\widehat{\bar{\mathbf{v}} \cdot \nabla \bar{\theta}})^N - \left(\frac{d\bar{\theta}}{dz} \right) \hat{v}_z^N \right] - \frac{1}{2} \left[-(\widehat{\bar{\mathbf{v}} \cdot \nabla \bar{\theta}})^{N-1} - \left(\frac{d\bar{\theta}}{dz} \right) \hat{v}_z^{N-1} \right]. \quad (29b)$$

The velocity and potential temperature are updated via:

$$\hat{\mathbf{v}}^{N+\frac{1}{4}} = \hat{\mathbf{v}}^N + \Delta t \left[\hat{\mathfrak{R}} + \hat{\mathbf{z}} \beta(z) \left(\frac{g}{\bar{\theta} \omega_B} \right) \hat{\mathfrak{M}} \right], \quad (30a)$$

$$\hat{\theta}^{N+\frac{1}{2}} = \hat{\theta}^N + \Delta t \left[\hat{\mathfrak{M}} - \beta(z) \left(\frac{\bar{\theta} \omega_B}{g} \right) \left(\hat{\mathfrak{R}}_z - \frac{\partial \hat{h}^N}{\partial z} \right) \right]. \quad (30b)$$

The function $\beta(z)$ determines the range of z at which the damping operates; $\beta(z) = 0$ for most of the domain, but will be nonzero and small in the low density regions.

We note that one could damp buoyant oscillations just by adding a term proportional to $-\bar{v}_z$ (instead of $\partial \bar{\theta} / \partial t$) to the vertical velocity equation, and/or a term proportional to $-\bar{\theta}$ (instead of $-\partial \bar{v}_z / \partial t$) to the potential temperature equation. However, the advantage of adding time derivatives is that as the flow approaches a steady-state, the damping naturally turns off. We will explore the effects of this gravity-wave damping mechanism in Section 4.3.

3.3.3. Step 2: Hyperviscosity

Unlike finite-difference codes which have a “grid viscosity” associated with the spatial differencing, spectral codes have no inherent grid dissipation. Energy will cascade down (via nonlinear interactions) to the smallest resolved scales (highest wavenumbers) where it will accumulate and eventually cause large truncation and aliasing errors. To control this, artificial viscosity or some other kind of low-pass filtering is applied to dissipate the energy at the smallest scales [13,10]. This method is related to “large-eddy” simulations in which the large scale motions are fully resolved, whereas the small scale flow is treated with a sub-grid scale turbulence model.

For the two horizontal Fourier directions, we apply a hyperviscosity of the form: $v_{\perp}^{\text{hyp}}(-1)^{p+1}\nabla_{\perp}^{2p}$, where v_{\perp}^{hyp} is a hyperviscosity coefficient, and p is an integer between 1 and 6. This is simple to implement because the hyperviscosity operator is an exact eigenoperator of the Fourier basis functions:

$$(-1)^{p+1}\nabla_{\perp}^{2p}\exp(ik_x x + ik_y y) = -(k_x^2 + k_y^2)^p \exp(ik_x x + ik_y y). \quad (31)$$

The vertical direction is not resolved with a Fourier basis and is not periodic. Applying a real diffusion operator to the vertical direction is problematic because the second derivative operator (or its powers) is not an eigenoperator of the Chebyshev polynomial or rational Chebyshev function bases. Furthermore, a real diffusion operator would raise the order of the differential equations and require additional unphysical vertical boundary conditions and/or create spurious boundary layers. Boyd [10] advocates replacing the second derivative operator with an eigenoperator of the basis functions. For example, for the Chebyshev polynomial basis (where we assume $L_z = 1$):

$$\frac{d^2}{dz^2} \rightarrow \sqrt{1-z^2} \frac{d}{dz} \left[\sqrt{1-z^2} \frac{d}{dz} \right], \quad (32a)$$

$$\sqrt{1-z^2} \frac{d}{dz} \left[\sqrt{1-z^2} \frac{d}{dz} \right] T_n(z) = -n^2 T_n(z). \quad (32b)$$

Likewise, there is a similar replacement for the eigenoperator of the rational Chebyshev function basis. Because the eigenoperators are singular at the boundaries, no additional unphysical boundary conditions are needed and no spurious boundary layers are created.

In practice, we apply hyperviscosity every timestep:

$$f_{\text{hyp}} \equiv \exp[-\Delta t(v_{\perp}^{\text{hyp}} k_{\perp}^{2p} + v_z^{\text{hyp}} k_z^{2p})], \quad (33a)$$

$$\hat{v}^{N+\frac{3}{4}} = \hat{v}^{N+\frac{1}{4}} \cdot f_{\text{hyp}}, \quad (33b)$$

$$\hat{\theta}^{N+1} = \hat{\theta}^{N+\frac{1}{2}} \cdot f_{\text{hyp}}, \quad (33c)$$

where $k_{\perp}^2 \equiv k_x'^2 + (k_y' + \sigma t k_x')^2$, $k_z \equiv \pi n/L_z$, and n is the order of the Chebyshev polynomial or rational Chebyshev function. The hyperviscosity coefficients are initially set to values such that the highest resolved Fourier or Chebyshev number has an e -folding time equal to one timestep. They can be dynamically adjusted every few hundred timesteps so that the energy spectrum does not curl-up at the highest wavenumbers.

3.3.4. Step 3: Poisson-like equation for pressure/enthalpy

Subtraction of the enthalpy gradient is done with a semi-implicit Crank–Nicholson (globally second-order in time) algorithm:

$$\hat{v}^{N+\frac{3}{4}} = \hat{v}^{N+\frac{1}{4}} - \frac{1}{2}\Delta t \hat{\mathbf{V}}^N \hat{h}^N, \quad (34a)$$

$$\hat{v}^{N+1} = \hat{v}^{N+\frac{3}{4}} - \frac{1}{2}\Delta t \hat{\mathbf{V}}^{N+1} \hat{h}^{N+1}, \quad (34b)$$

where $\hat{\mathbf{V}}^N \equiv [ik_x', i(k_y' + \sigma t k_x'), \partial/\partial z]$. Step (34a), the explicit step, uses the current enthalpy, whereas step (34b), the implicit step, uses the future enthalpy. We require that the final velocity satisfy the anelastic constraint, which yields a Poisson-like equation for the final enthalpy:

$$\left[\hat{\mathbf{v}}^{N+1} + \left(\frac{d \ln \bar{\rho}}{dz} \right) \hat{\mathbf{z}} \right] \cdot \hat{\mathbf{v}}^{N+1} = 0, \tag{35a}$$

$$\left[\frac{\partial^2}{\partial z^2} + \left(\frac{d \ln \bar{\rho}}{dz} \right) \frac{\partial}{\partial z} - (k_{\perp}^{N+1})^2 \right] \hat{h}^{N+1} = \frac{2}{\Delta t} \left[\hat{\mathbf{v}}^{N+1} + \left(\frac{d \ln \bar{\rho}}{dz} \right) \hat{\mathbf{z}} \right] \cdot \hat{\mathbf{v}}^{N+\frac{3}{4}}, \tag{35b}$$

where $(k_{\perp}^{N+1})^2 \equiv k_x'^2 + (k_y' + \sigma t^{N+1} k_x')^2$.

If the vertical domain is finite (i.e., Chebyshev polynomial basis), then explicit boundary conditions will be needed to solve this Poisson-like equation. We require that the vertical velocity vanish at the walls. Imposing this on the z -component of (34b) yields:

$$\hat{v}_z^{N+1} \Big|_{z=\pm L_z} = 0, \tag{36a}$$

$$\frac{\partial \hat{h}^{N+1}}{\partial z} \Big|_{z=\pm L_z} = \frac{2}{\Delta t} \hat{v}_z^{N+\frac{3}{4}} \Big|_{z=\pm L_z}. \tag{36b}$$

If the vertical domain is infinite (i.e., rational Chebyshev function basis), then no explicit boundary conditions are needed to invert the Poisson-like equation because the vertical basis functions individually satisfy the boundary conditions (i.e., Galerkin method with natural boundary conditions): $dC_n(z)/dz \rightarrow 0$ and $S_n(z) \rightarrow 0$ as $z \rightarrow \pm\infty$.

The Poisson-like equation is singular for the case of $k_x' = k_y' = 0$. The anelastic condition for this mode implies that there can be no net vertical momentum across any horizontal plane:

$$\hat{v}_{z,00}^{N+1} = 0, \tag{37a}$$

$$\frac{\partial \hat{h}_{00}^{N+1}}{\partial z} = \frac{2}{\Delta t} \hat{v}_{z,00}^{N+\frac{3}{4}}. \tag{37b}$$

The integration constant for \hat{h}^{N+1} is determined by the condition that the total mass in the domain is conserved.

One can write the Poisson-like equation (35b) in matrix form: $\mathbb{M} \hat{\mathbf{h}} = \hat{\mathbf{g}}$, where \mathbb{M} is a matrix containing the Laplacian-like differential operator, $\hat{\mathbf{h}}$ is a column vector of vertical spectral coefficients for the enthalpy, and $\hat{\mathbf{g}}$ is a column vector of vertical spectral coefficients for the right-hand side of (35b). When needed, the last two rows of the matrix \mathbb{M} are overwritten with the boundary condition data (36b), at the expense that the divergence condition will not be satisfied for the two highest vertical spectral modes. This is usually an exponentially small error, but if it is undesirable, one can use the tau-method with Greens functions to correct the divergence at the two highest spectral modes (see Appendix B; [29]).

The speed and efficiency in inverting the Poisson-like equation depends on the functional form of the stratification term $d \ln \bar{\rho}/dz$. If the stratification term is particularly simple (e.g., zero for no stratification, a constant for constant stratification, or proportional to height z as in a protoplanetary disk), then one can use Chebyshev or rational Chebyshev recursion relations; the matrices will be banded and consequently quick to invert. In particular, for the finite domain with the Chebyshev polynomial basis, the matrix equation can be rewritten as: $\mathbb{A} \hat{\mathbf{h}} = \mathbb{B} \hat{\mathbf{g}}$, where \mathbb{A} and \mathbb{B} are pentadiagonal matrices (see Appendix A, [13,23]). If the stratification term is an odd function of z , then the even and odd Chebyshev modes decouple, reducing the pentadiagonal matrix equation to two tridiagonal matrix equations for the even and odd Chebyshev modes. For the infinite domain with rational Chebyshev function basis, the matrix \mathbb{M} is nonadiagonal (see Appendix C). If the stratification term is an odd function of z , then the even and odd rational Chebyshev modes decouple, reducing the nonadiagonal matrix equation to two pentadiagonal matrix equations for the even and odd rational Chebyshev modes. On the other hand, if the stratification term is a more complicated function of height, then the terms multiplied by the stratification term will have to be computed in physical space on a grid of collocation points, and then transformed back to function space. The matrices in the Poisson-like equation will consequently be full and slower to invert.

4. Numerical tests

4.1. Parallelization and timing analysis

We have developed our simulation for use on parallel supercomputers such as the Blue Horizon (decommissioned in April 2004) and DataStar supercomputers at the San Diego Supercomputer Center. The DataStar has 176 nodes of 8 processors (CPU speed of 1.5 GHz and peak performance of 6.0 GFlops). Each node shares 16 GB of memory.

Different horizontal Fourier modes interact only through the nonlinear advection terms, whereas the vertical spectral modes (Chebyshev polynomials or rational Chebyshev functions) are fully coupled at every stage of the computation. This motivated us to divide the computational domain only along the horizontal directions. Each processor works with a small subset of horizontal data, but all of the corresponding vertical data: in physical space, the j th processor would contain data for: $x_1^j \leq x < x_2^j, y_1^j \leq y < y_2^j, -L_z \leq z \leq +L_z$; in wave-number space, a given processor would contain data for: $k_{x,1}^j \leq k_x < k_{x,2}^j, k_{y,1}^j \leq k_y < k_{y,2}^j, 0 \leq n \leq N_z$. The only time different processors communicate with each other is when a horizontal FFT needs to be computed. There are generally two common strategies for this: one could use a FFT that works across processors, or one could transpose the data so that a given direction is not split across processors. For example, if one wanted to compute a FFT along the x direction, one would swap the data so that each processor had a subset of the y and z data, but all of the corresponding x data. We have implemented this second strategy with an efficient transpose algorithm developed by Alan Wray at NASA-Ames/Stanford Center for Turbulence Research (Wray, personal communication).

Fig. 4 shows the results of timing tests for a version of the code that used the Chebyshev polynomial basis. The tests were done on the Blue Horizon and analyzed with the Vampir parallel trace tool. For reference, we note that the DataStar runs approximately two times faster than the Blue Horizon. We present the average

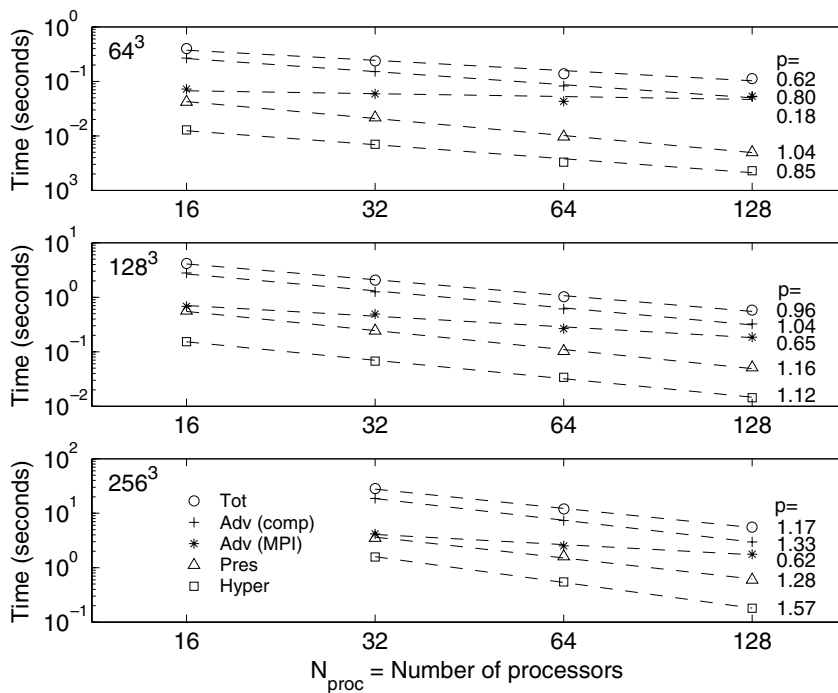


Fig. 4. Average wall-clock or real time to compute one timestep using 16, 32, 64, and 128 processors on the IBM Blue Horizon at the San Diego Supercomputer Center. Parallelization is implemented with the message passing interface (MPI) protocol. ‘Tot’ = Total time for one timestep, ‘Adv (comp)’ = computation time for advection step, ‘Adv (MPI)’ = MPI communication time for advection step, ‘Pres’ = computation time for pressure step, ‘Hyper’ = computation time for hyperviscosity step. The dashed lines are power-law fits; the numbers to the right of the data are the best-fit exponent: $\text{Time} \propto N_{\text{proc}}^{-p}$. For reference, we note that the DataStar runs approximately two times faster than the Blue Horizon.

wall-clock or real time to compute one timestep for 64^3 , 128^3 , and 256^3 domains on 16, 32, 64, and 128 processors. We fit power laws ($T \propto N_{\text{proc}}^{-p}$) to the timing data and determined how the times for different steps in the algorithm scale with number of processors (ideal performance is $p \approx 1$). As expected, the advection step is the most time-intensive step in the algorithm: 80–90% of the time is spent in this stage alone due to the large number of FFTs required to compute the nonlinear terms. The computation time (‘Adv comp’) scales well with the number of processors, whereas the communication time (‘Adv MPI’) has a much flatter scaling.

4.2. 2D elliptical vortex in a shearing flow

To validate the shearing box algorithm, we simulate a 2D elliptical vortex in a shearing flow. Moore and Saffman [36] analytically determined the steady state solution for a 2D elliptical vortex of uniform vorticity $\tilde{\omega}_z$ embedded in a uniform shear of strength σ , and showed that the aspect ratio of the vortex, $\chi \equiv A_x/A_y$, where A_x and A_y are the major and minor axes of the ellipse, was determined by the ratio of the vorticity to the shear:

$$\frac{\tilde{\omega}_z}{\sigma} = \left(\frac{\chi + 1}{\chi - 1} \right) \frac{1}{\chi}, \tag{38}$$

which is valid for vortices that rotate in the same sense as the shear. As one would expect, stronger vortices are more round and compact, whereas weaker vortices are more elongated. Kida [25] showed that if such a vortex was perturbed, its major axis would oscillate about the x -axis, and its aspect ratio would oscillate about its mean value (area remaining constant). These motions would be damped via the occasional shedding of thin filaments of vorticity which would eventually be dissipated by viscosity.

Fig. 5 shows the kinetic, shear, and total energies as a function of time for the evolution of a 2D elliptical vortex. The parameters for these runs were: $(L_x, L_y) = (4, 2)$, $(N_x, N_y) = (256, 128)$, $\Omega = 1$, $\sigma = -1.5$, $t_{\text{rm}} = 4/3$, $\Delta t = t_{\text{rm}}/100$, $(A_x, A_y) = (1, 0.25)$, $\tilde{\omega}_z(0) = -0.625$. The initial vortex was surrounded with a weak halo of oppositely-oriented vorticity so that there was no net circulation around the vortex ($\Gamma \equiv \int_A \tilde{\omega}_z \, dx \, dy = 0$). The Kida oscillations are readily apparent in the energy plots as the larger amplitude, longer period oscillations (≈ 8 re-map periods). As expected, increasing the hyperviscosity resulted in the damping of these oscillations; the final state is a steady-state vortex whose major axis is aligned with the x -axis and whose aspect ratio and area are constant.

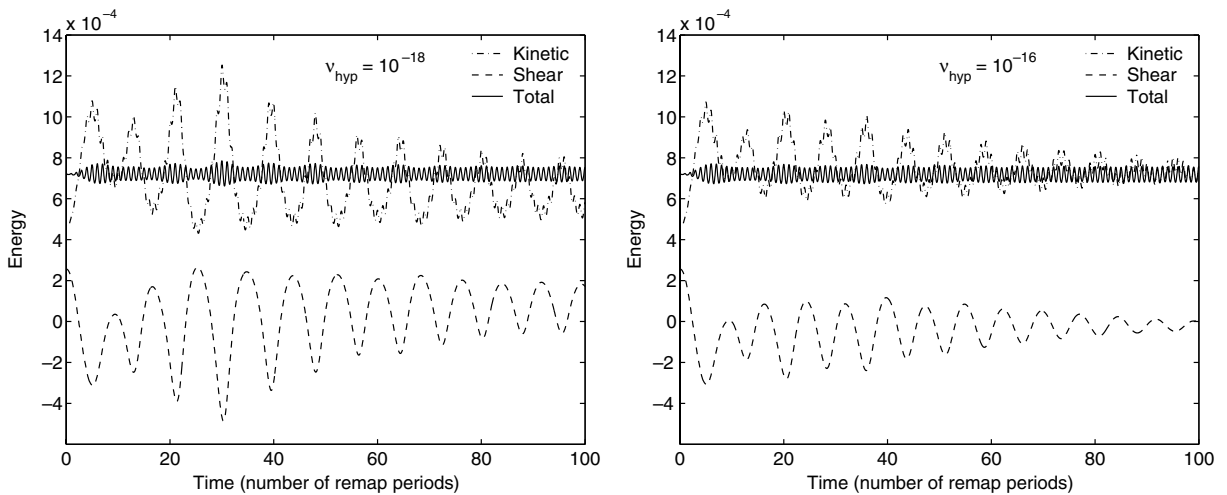


Fig. 5. Kinetic, shear, and total energy for 2D elliptical vortex embedded in a linear shear: (a) $v_{\text{hyp}} = 10^{-18}$ with $2p = 12$, (b) $v_{\text{hyp}} = 10^{-16}$ with $2p = 12$. The larger amplitude, longer period (≈ 8 re-map periods) oscillations are associated with the major axis of the vortex oscillating about the x -axis and with the aspect ratio oscillating around its mean value, as described by Kida [25]. The lower-amplitude, shorter period oscillations (exactly equal to the re-map period) are due to interactions with the periodic image vortices, which are realigned with the primary vortex every re-map period. The Kida oscillations are damped via the shedding of thin filaments which are dissipated by hyperviscosity.

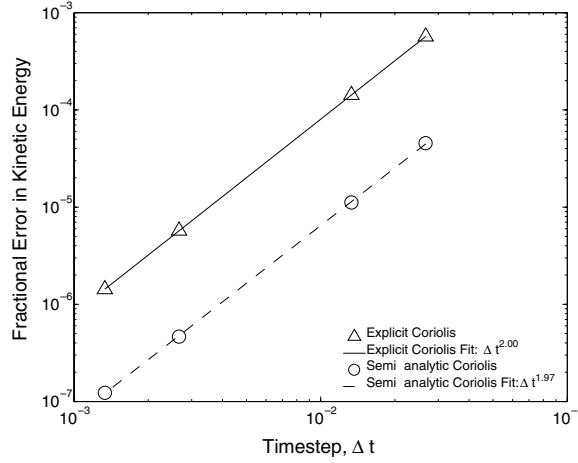


Fig. 6. Fractional error in final kinetic energy after one re-map period versus timestep size for explicit and semi-analytic treatments of the Coriolis force. Both methods are second-order accurate, but the error is an order of magnitude smaller for the semi-analytic method.

Superposed on the Kida oscillations is another low amplitude, short period oscillation, which is most clearly seen in the plots of total energy. This period is exactly the re-map period and is due to interactions of the vortex with its periodic images, which are realigned with the primary vortex every re-map period (see Fig. 2). The amplitude of these oscillations decreases with domain size.

In Fig. 6, we plot the fractional error in kinetic energy after one re-map period as a function of timestep size for the explicit and semi-analytic treatments of the Coriolis (modified by shear) terms. We fit power-laws and confirmed that both schemes are globally second-order accurate in time. The semi-analytic treatment, however, has an error that is an order of magnitude smaller than the explicit scheme. This is, perhaps, not surprising. If we were to re-write the algorithms as Taylor series expansions around a particular time t_0 , the neglected terms are of order Δt^3 . However, the scaling with timestep is not the whole story. Although both algorithms drop terms of the same order, the semi-analytic treatment naturally captures the oscillatory behavior of the Coriolis and buoyancy forces, so that apparently, the magnitudes of the neglected terms are smaller.

4.3. Linear eigenmodes in a stratified protoplanetary disk

To test the vertical dimension of the code, we investigate the behavior of linear eigenmodes (i.e., internal gravity waves) in a stratified background. The background shear makes it difficult to compute eigenmodes because the linearized equations depend explicitly on $\sigma y \partial / \partial x$ in the original coordinates, or explicitly on $\sigma t i k_x$ in the shearing coordinates. If we restrict the following analysis to the case of $\partial / \partial x = i k_x = 0$, then the process of finding eigenmodes is straightforward. We look for eigenmodes of the form $\hat{q}(z) \exp(i k_y y - i \omega t)$, where q represents any variable. The real part of the eigenvalue is related to the phase speed of the wave, $c = \Re(\omega) / k_y$, whereas the imaginary part $\gamma = \Im(\omega)$ corresponds to wave growth (if positive) or damping (if negative). The linearized equations are:

$$-i\omega \hat{v}_x = (2\Omega + \sigma) \hat{v}_y, \quad (39a)$$

$$-i\omega \hat{v}_y = -2\Omega \hat{v}_x - i k_y \hat{h}, \quad (39b)$$

$$-i\omega \hat{v}_z = -d\hat{h}/dz + (\hat{\theta}/\bar{\theta})g - \beta\omega_B \hat{v}_z, \quad (39c)$$

$$-i\omega \hat{\theta} = -(d\bar{\theta}/dz) \hat{v}_z - \beta\omega_B [\hat{\theta} - (\bar{\theta}/g) d\hat{h}/dz], \quad (39d)$$

$$0 = i k_y \hat{v}_y + d\hat{v}_z/dz + (d \ln \bar{\rho}/dz) \hat{v}_z, \quad (39e)$$

where we have included the damping terms described in Section 3.3.2. If the damping terms are neglected, then this system of equations can be simplified to the second-order eigenvalue problem for the vertical velocity fluctuation:

$$\left(\frac{\omega}{\omega_C}\right)^2 \left[\mathcal{L} - k_y^2\right] \hat{v}_z = \left[\mathcal{L} - k_y^2 \left(\frac{\omega_B}{\omega_C}\right)^2\right] \hat{v}_z, \tag{40}$$

where we have defined the second-order linear differential operator:

$$\mathcal{L}f \equiv \frac{d}{dz} \left[\frac{df}{dz} + \left(\frac{d \ln \bar{\rho}}{dz} \right) f \right]. \tag{41}$$

If the eigenvalue problem is solved on the finite domain with the Chebyshev polynomial basis, then boundary conditions must be imposed: $\hat{v}_z(z = \pm L_z) = 0$. On the infinite domain with the rational Chebyshev function basis, boundary conditions are naturally satisfied by the basis functions (i.e., Galerkin method).

In order to proceed, we need to specify the background state. Here, we choose conditions relevant to a protoplanetary disk of gas and dust in orbit around a newly-formed protostar [8,7]. The velocity profile of the gas is very nearly Keplerian: $V_K(r) \equiv r\Omega_K(r) \equiv \sqrt{GM_\star}/r$, where G is the gravitational constant, M_\star is the mass of the protostar, and r is the cylindrical radius to the protostar. The horizontal shear rate of this base flow is: $\sigma_K \equiv r(\partial\Omega_K/\partial r) = -(3/2)\Omega_K$. Keplerian shear is anticyclonic (as indicated by the negative sign), and is comparable in magnitude to the rotation rate itself. We do not simulate the entire disk; rather, we simulate the hydrodynamics only within a small patch ($\Delta r \ll r_0, \Delta\phi \ll 2\pi$) that co-rotates with the gas at some fiducial radius r_0 with angular velocity $\Omega_0 \equiv \Omega(r_0)$. We map this patch of the disk onto a Cartesian grid: $r - r_0 \rightarrow y$, $r_0(\phi - \phi_0) \rightarrow -x$, $z \rightarrow z$, $v_r \rightarrow v_y$, $v_\phi \rightarrow -v_x$, and $v_z \rightarrow v_z$. In this rotating patch, the velocity profile of the

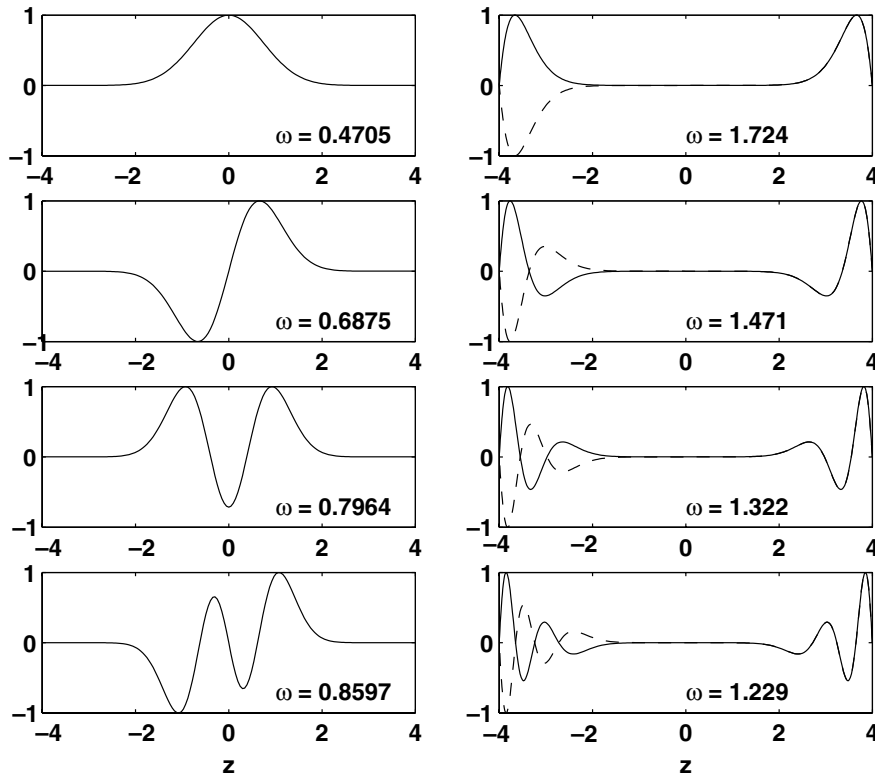


Fig. 7. Vertical velocity component of the undamped ($\beta = 0$) eigenmodes in a stratified protoplanetary disk. Units are chosen so that $H_0 = \Omega_0 = 1$. Horizontal wavenumbers for these modes are: $(k_x, k_y) = (0, \pi/H_0)$. There are two kinds of eigenmodes: those localized around the weakly stratified midplane with frequencies $\omega < \Omega_0$ (left column), and those localized in the strongly stratified regions near the boundaries with frequencies $\omega > \Omega_0$ (right column). In the right column, the boundary modes are doubly degenerate: the symmetric modes are shown with solid lines, the antisymmetric modes are shown with dashed lines.

gas is very nearly a linear shear flow with $\sigma_0 \equiv \sigma_K(r_0) = -(3/2)\Omega_0$. The Coriolis frequency (modified by the shear) is $\omega_C = \Omega_0$.

The vertical component of the protostellar gravity in this patch of the disk is very nearly $g_z(z) \approx \Omega_0^2 z$. We assume that the background is constant temperature $\bar{T} = T_0$, which yields a hydrostatic density profile that is Gaussian:

$$\bar{\rho}(z) = \rho_0 \exp(-z^2/2H_0^2), \quad H_0^2 \equiv \mathcal{R}T_0/\Omega_0^2, \quad (42a)$$

$$H_\rho(z) \equiv |(d \ln \bar{\rho}/dz)^{-1}| = H_0^2/|z|. \quad (42b)$$

The Brunt–Väisälä frequency is:

$$\omega_B(z) = \sqrt{\mathcal{R}/C_p \Omega_0 |z|/H_0}. \quad (43)$$

The disk can be divided into two regimes: a nearly unstratified midplane ($\omega_B < \Omega_0$, $|z|/H_0 \lesssim 1.6$) and a strongly stratified atmosphere above and below the midplane ($\omega_B > \Omega_0$, $|z|/H_0 \gtrsim 1.6$).

Fig. 7 shows the vertical velocity component of the undamped ($\beta = 0$) eigenmodes for $k_y H_0 = \pi$. The eigenvalues are purely real. There are two kinds of eigenmodes: those confined to the weakly stratified midplane of

Table 1
Effect of damping on linear eigenmodes

β_{\max}	$\omega = 0.8597$	$\omega = 1.229$
0	0.8597	1.229
10^{-4}	$0.8597 - i3.446 \times 10^{-11}$	$1.229 - i1.601 \times 10^{-5}$
10^{-3}	$0.8597 - i3.956 \times 10^{-10}$	$1.229 - i1.601 \times 10^{-4}$
10^{-2}	$0.8597 - i3.975 \times 10^{-9}$	$1.229 - i1.601 \times 10^{-3}$
10^{-1}	$0.8597 - i3.946 \times 10^{-8}$	$1.231 - i1.600 \times 10^{-2}$
1	$0.8597 - i3.945 \times 10^{-7}$	$1.302 - i1.148 \times 10^{-1}$

An eigenmode that is localized near the midplane (e.g., $\omega = 0.8597\Omega_0$) is weakly damped, whereas an eigenmode that is localized far from the midplane (e.g., $\omega = 1.229\Omega_0$) is strongly damped. Damping rate is linearly proportional to β_{\max} .

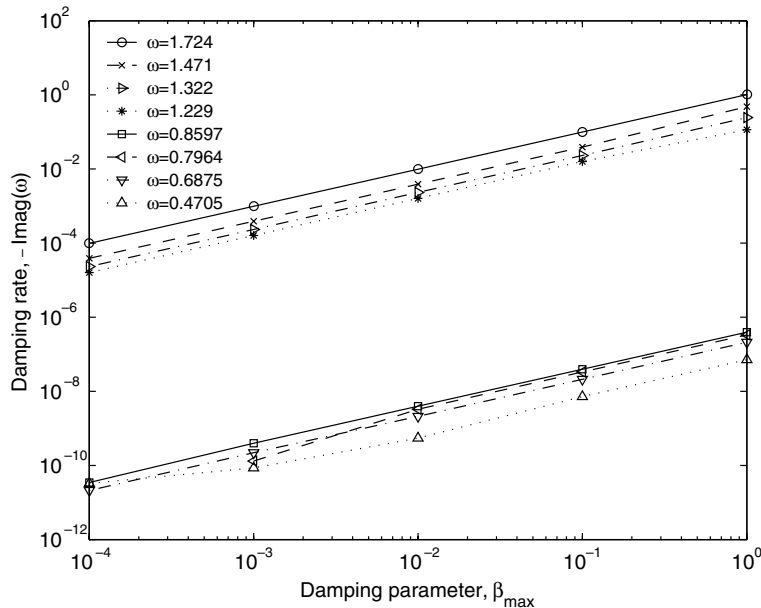


Fig. 8. Numerically computed damping rate for linear eigenmodes as a function damping parameter β_{\max} . Eigenmodes that are localized near the midplane (lower group) are weakly damped, whereas eigenmodes that are localized far from the midplane (upper group) are strongly damped. Damping rate is very nearly linearly proportional to β_{\max} .

the disk with frequencies $\omega < \Omega_0$, and those confined to the strongly stratified regions near the boundaries with frequencies $\omega > \Omega_0$. The latter class of eigenmodes do not exist when the domain is infinite (rather, there is a continuous spectrum of waves whose velocity amplitudes are formally unbounded as $|z| \rightarrow \infty$).

To investigate the effect of damping on these eigenmodes, we need to specify a profile for $\beta(z)$, for example:

$$\beta(z) = \beta_{\max} \{1 + 0.5 \tanh[a(z - z_c)/H_0] - 0.5 \tanh[a(z + z_c)/H_0]\}, \tag{44}$$

which is nearly zero for most of the domain, but rises sharply at $|z| \approx z_c$ to its maximum value β_{\max} ; the parameter a sets how steep the rise is. In the calculations presented here, we take $a = 4$ and $z_c = 3H_0$. Table 1 and Fig. 8 show the effect of varying β_{\max} on the two kinds of eigenmodes. Those eigenmodes that are localized around the midplane are only weakly damped, whereas the eigenmodes that are localized in the strongly stratified regions near the boundary are strongly damped.

In fully nonlinear 3D calculations, this damping is necessary for numerical stability. As internal gravity waves propagate from a high density regions into low density regions, their amplitudes increase so as to conserve energy flux, causing velocity and thermodynamic fluctuations that can become sufficiently large so as to invalidate the anelastic approximation and/or violate the CFL condition.

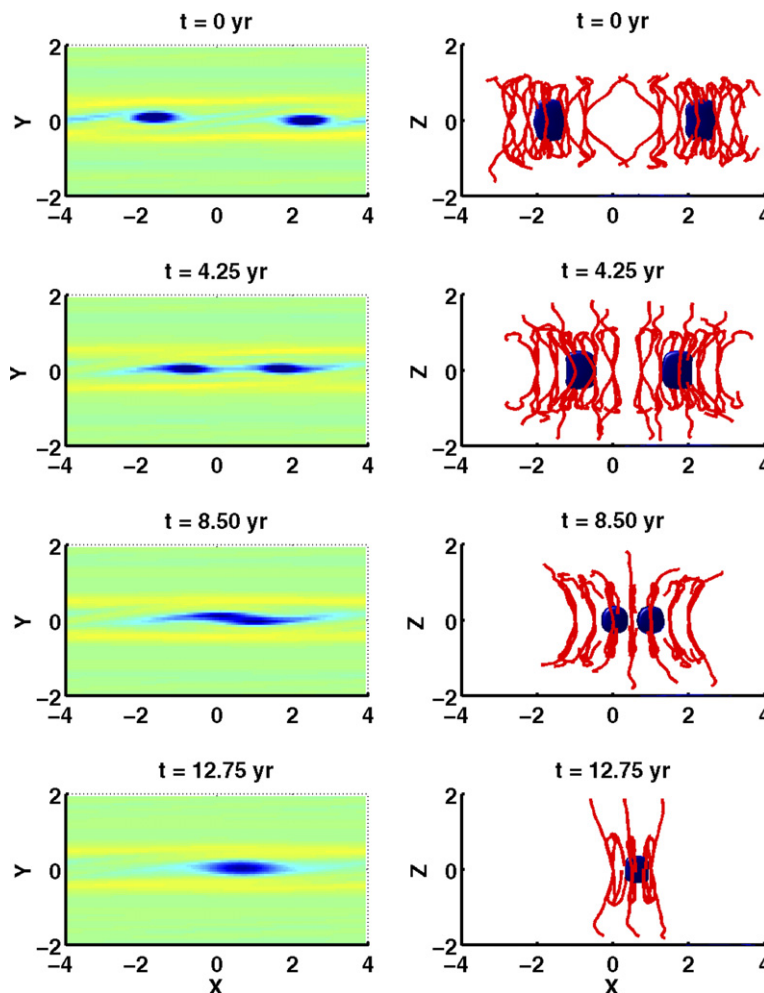


Fig. 9. The merger of two 3D vortices in the midplane of a protoplanetary disk. In the first column, we show x - y slices in the midplane $z = 0$ of the z -component of vorticity. Blue corresponds to anticyclonic vorticity, red corresponds to cyclonic vorticity. In the second column, we present isovorticity surfaces for the z -component of vorticity in blue, and vortex lines (lines that are everywhere tangent to the vorticity vector) in red. Units of time: $\tau_{\text{orb}} \equiv 2\pi/\Omega_0 = 1$ yr.

4.4. Merger of two 3D vortices in a protoplanetary disk

As a preview of potential applications, we present the simulation of a merger of two 3D vortices in the midplane of a stratified protoplanetary disk. A more complete discussion of simulations of vortices in protoplanetary disks can be found in [7,8]. We use the 2D vortex solution of Moore and Saffman [36], and Kida [25] to initialize an elliptical vortex in the midplane at $z = 0$. The vorticity is extended off the midplane according to a Gaussian profile:

$$\tilde{\omega}_z(z) = \tilde{\omega}_z(0)e^{-z^2/2H_0^2}. \quad (45)$$

We initialize the temperature so that the buoyancy force exactly balances the vertical pressure force:

$$\tilde{T} = \frac{T_0}{\Omega_0^2 z} \frac{\partial(\tilde{p}/\bar{\rho})}{\partial z}. \quad (46)$$

Of course, only under very special circumstances would this procedure just so happen to also exactly balance the temperature equation. In general, $\partial\tilde{T}/\partial t \neq 0$ initially, leading to an immediate evolution of the temperature. Vertical motions will then be generated by the temperature changes through the buoyancy force, and these vertical velocities will then couple the horizontal motions at different heights. We allow such a 3D vortex to evolve and relax to a quasi-equilibrium. We then use that vortex as a template to construct an initial condition with two vortices destined to merge.

Fig. 9 shows an example of a merger. The parameters for this run were: $(L_x, L_y, L_z) = (8, 4, 8)$, $(N_x, N_y, N_z) = (128, 64, 128)$, $H_0 = 1$, $\Omega = 1$, $\sigma = -1.5$, $t_{\text{rm}} = 4/3$, $(A_x, A_y) = (1, 0.25)$, $\tilde{\omega}_z(0) = -0.625$. Hyperviscosity with order $2p = 8$ was used to damp the smallest scales. The first column shows x - y slices in the midplane $z = 0$ of the z -component of vorticity. Blue corresponds to anticyclonic vorticity, red corresponds to cyclonic vorticity. The second column shows isovorticity surfaces for the z component of vorticity, in blue, and vortex lines (lines that are everywhere tangent to the vorticity vector) in red. The vorticity field is divergence-free (since it is the curl of another vector field). Thus, like magnetic field lines, vortex lines cannot begin or end in free space, they must either end on a boundary, extend to infinity, form closed loops, or form unending open curves.

In Fig. 10, we show the fractional error in the kinetic energy after one re-map time as a function of timestep size, for 3D simulations of merging vortices. As was the case in Fig. 6 for 2D simulations, both the explicit and

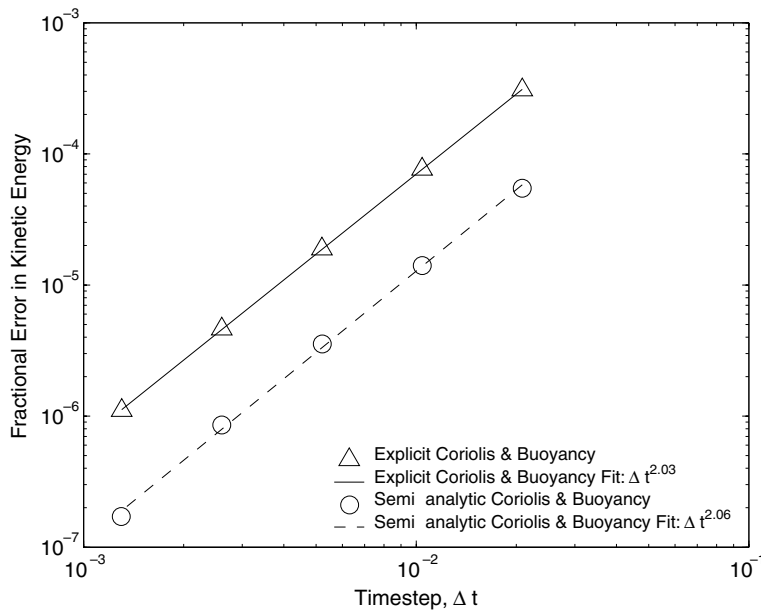


Fig. 10. Fractional error in final kinetic energy after one re-map period versus timestep size for explicit and semi-analytic treatments of the Coriolis and buoyancy forces. Both methods are second-order accurate, but the error is an order of magnitude smaller for the semi-analytic method.

semi-analytic algorithms are globally second-order accurate, but the semi-analytic treatment has an error almost an order of magnitude smaller.

5. Conclusion

We have developed a three-dimensional (3D) spectral hydrodynamic code to study vortex dynamics in rapidly rotating, intensely sheared, and strongly stratified systems. The code integrates a number of specially tailored algorithms to handle the numerical challenges associated with shear and stratification. We use the anelastic approximation to filter sound waves and shocks. The horizontal coordinates are transformed to a set of shearing coordinates that advect with the background shear flow, and a Fourier–Fourier basis in these shearing coordinates is used for spectral expansions in the two horizontal directions. For the vertical direction, two different sets of basis functions have been implemented: (1) Chebyshev polynomials on a truncated, finite domain, and (2) rational Chebyshev functions on an infinite domain. The nonlinear advection terms are time integrated explicitly, whereas the enthalpy gradient is integrated semi-implicitly. The Coriolis and buoyancy terms can be treated either explicitly or semi-analytically. We show that gravity waves can also be damped by adding new terms to the Euler equations. The code is parallelized with the message passing interface (MPI), and we get excellent parallel performance on the IBM Blue Horizon and Datastar supercomputers at the San Diego Supercomputer Center.

Although we believe this code can be applied to a wide set of problems in astrophysical and geophysical fluid dynamics, we would like to point out a number of limitations. First, the anelastic approximation limits its validity to flows that are subsonic. Fully compressible equations can, in principle, be treated with modifications to the time integration algorithms; special care will be needed to handle any shocks that may develop. Second, if the fluctuations on the background shear become so large as to significantly alter the shear profile itself, the shearing coordinates and re-mapping algorithms may perform poorly (e.g., large aliasing errors). In these cases, the shearing sheet formalism should be discarded in favor of global simulations that allow for both the background flow and fluctuations to evolve in time.

A future version of the code will include the effects of magnetic fields. This will involve the induction equation for the evolution of the magnetic field and the addition of the Lorentz force to the equation for momentum balance:

$$\left(\frac{\partial}{\partial t} - \sigma y \frac{\partial}{\partial x}\right) \tilde{\mathbf{v}} = \dots + \frac{1}{4\pi\rho} (\nabla \times \mathbf{B}) \times \mathbf{B}, \quad (47a)$$

$$\left(\frac{\partial}{\partial t} - \sigma y \frac{\partial}{\partial x}\right) \mathbf{B} = -\sigma B_y \hat{\mathbf{x}} + \nabla \times (\tilde{\mathbf{v}} \times \mathbf{B}). \quad (47b)$$

The divergence-free condition $\nabla \cdot \mathbf{B} = 0$ can be enforced by defining the magnetic field in terms of a poloidal–toroidal decomposition:

$$\mathbf{B} \equiv \nabla \times (\psi \hat{\mathbf{z}}) + \nabla \times \nabla \times (\chi \hat{\mathbf{z}}), \quad (48)$$

where ψ is the toroidal scalar field and χ is the poloidal scalar field [15].

Acknowledgments

J.A.B. thanks the National Science Foundation for support via a Graduate Student Fellowship while at Berkeley, and now with an Astronomy and Astrophysics Postdoctoral Fellowship (NSF Grant AST0302146). He also thanks the support of the Kavli Institute for Theoretical Physics through NSF Grant PHY9907949. P.S.M. thanks the support of NASA Grant NAG510664 and NSF Grant AST0098465. Computations were carried out at the San Diego Supercomputer Center using an NPACI award. The authors also thank Andrew Szeri, Xylar Asay-Davis, and Sushil Shetty for useful comments on the early manuscript.

Appendix A. Solving the Poisson-like equation for the enthalpy with Chebyshev polynomial basis (“tau method”)

For the case where the stratification is a linear function of height z , the Poisson-like equation for the enthalpy (35) can be written in the form:

$$\mathcal{M}f(z) \equiv \left[\frac{d^2}{dz^2} - \gamma z \frac{d}{dz} - \lambda \right] f(z) = g(z), \quad (\text{A.1a})$$

$$\left. \frac{df}{dz} \right|_{z=\pm 1} = \chi_{\pm}, \quad (\text{A.1b})$$

where we have chosen dimensions so that the boundaries are located at $z = \pm 1$. There will be one such equation for each pair of horizontal wavenumbers $\{k'_x, k'_y\}$. We expand $f(z)$ and $g(z)$ in Chebyshev polynomial series:

$$f(z) = \sum_{n=0}^N \hat{f}_n T_n(z) \quad \text{and} \quad g(z) = \sum_{n=0}^N \hat{g}_n T_n(z). \quad (\text{A.2})$$

One can then use Chebyshev recursion relations to write the above Poisson-like equation in matrix form:

$$\mathbb{M}\hat{\mathbf{f}} = \hat{\mathbf{g}}, \quad (\text{A.3a})$$

$$\sum_{n=1}^N (\pm 1)^n n^2 \hat{f}_n = \chi_{\pm}, \quad (\text{A.3b})$$

where \mathbb{M} is a $(N+1) \times (N+1)$ matrix for the second-order linear differential operator \mathcal{M} , and $\hat{\mathbf{f}}$ and $\hat{\mathbf{g}}$ are column vectors of $N+1$ Chebyshev spectral coefficients. There are two problems with this formulation: the matrix \mathbb{M} is singular and the system is overspecified. We have $N+1$ undetermined spectral coefficients, but $N+3$ constraints ($N+1$ equations +2 boundary conditions). The tau method fixes both problems simultaneously by discarding the equations for the two highest Chebyshev modes and replacing them with the boundary conditions, resulting in the differential equation not being satisfied for those same two highest modes. The matrix \mathbb{M} is upper triangular (except for the last two rows which now contain boundary conditions) and fast to invert, but unfortunately is not diagonally dominant. The largest elements occur down the last column, and inverting it in its current form will have large round-off errors. Gottlieb and Orszag [23], and Canuto et al. [13] show how to rewrite the Poisson-like matrix equation in the form:

$$\mathbb{A}\hat{\mathbf{f}} = \mathbb{B}\hat{\mathbf{g}}, \quad (\text{A.4})$$

where \mathbb{A} and \mathbb{B} are diagonally dominant, pentadiagonal matrices. Gottlieb and Orszag [23], and Canuto et al. [13] give the recursion relations for the case $\gamma = 0$. Here, we present the recursion relation for the more general case:

$$c_{n-2}\hat{f}_{n-2} + c_n\hat{f}_n + c_{n+2}\hat{f}_{n+2} = d_{n-2}\hat{g}_{n-2} + d_n\hat{g}_n + d_{n+2}\hat{g}_{n+2}, \quad \text{for } 2 \leq n \leq N, \quad (\text{A.5})$$

where we have defined:

$$\begin{aligned} c_{n-2} &\equiv -\frac{\alpha_{n-2}\lambda + (n-2)\gamma}{4n(n-1)}, & d_{n-2} &\equiv \frac{\alpha_{n-2}}{4n(n-1)}, \\ c_n &\equiv 1 + \frac{\beta_{n+2}(\lambda - \gamma) - (1 - \beta_{n+2})\gamma(n+1)}{2(n^2 - 1)}, & d_n &\equiv -\frac{\beta_{n+2}}{2(n^2 - 1)}, \\ c_{n+2} &\equiv -\frac{\beta_{n+4}\lambda - \beta_{n+2}(2 - \beta_{n+4})\gamma(n+2)}{4n(n+1)}, & d_{n+2} &\equiv \frac{\beta_{n+4}}{4n(n+1)}, \end{aligned} \quad (\text{A.6})$$

and

$$\alpha_n \equiv \begin{cases} 2 & \text{for } n = 0, \\ 1 & \text{for } n \neq 0, \end{cases} \quad \text{and} \quad \beta_n \equiv \begin{cases} 1 & \text{for } n \leq N, \\ 0 & \text{for } n > N. \end{cases} \quad (\text{A.7})$$

The boundary conditions can be rewritten as:

$$\sum_{\substack{n=2 \\ n \text{ even}}}^N n^2 \hat{f}_n = \frac{\chi_+ + \chi_-}{2} \quad \text{and} \quad \sum_{\substack{n=1 \\ n \text{ odd}}}^N n^2 \hat{f}_n = \frac{\chi_+ - \chi_-}{2}. \quad (\text{A.8})$$

Note that the even and odd Chebyshev polynomials are decoupled in the matrix equation and in the boundary conditions, so one could in fact write the pentadiagonal system as two sets of tridiagonal systems for the even and odd modes.

Appendix B. Greens functions method to correct divergence condition for two highest Chebyshev modes

In [Appendix A](#), we presented a method to solve the Poisson-like equation for the enthalpy in a Chebyshev polynomial basis, subject to the constraint that the vertical velocity vanish at the two boundaries at $z = \pm 1$. The last two rows of the Poisson-like matrix equation were overwritten with boundary condition data, resulting in the anelastic divergence condition not being satisfied for the two highest Chebyshev modes. Here, we present a method to correct the divergence condition at the two highest modes using Greens functions [\[29\]](#), at the expense that equation for the evolution of the vertical momentum will not be satisfied at those same two highest modes.

To make the presentation more clear, we will first define a number of operators:

$$D \equiv (d/dz), \quad (\text{B.1a})$$

$$D_A \equiv (d/dz) + (d \ln \bar{\rho}/dz), \quad (\text{B.1b})$$

$$\hat{\mathbf{V}}^{N+1} \equiv i k'_x \hat{\mathbf{x}} + i(k'_y + \sigma t^{N+1} k'_x) \hat{\mathbf{y}} + D \hat{\mathbf{z}}, \quad (\text{B.1c})$$

$$\hat{\mathbf{V}}_A^{N+1} \equiv i k'_x \hat{\mathbf{x}} + i(k'_y + \sigma t^{N+1} k'_x) \hat{\mathbf{y}} + D_A \hat{\mathbf{z}}, \quad (\text{B.1d})$$

$$\Delta_A^{N+1} \equiv \hat{\mathbf{V}}_A^{N+1} \cdot \hat{\mathbf{V}}^{N+1}. \quad (\text{B.1e})$$

In the fourth fractional step [\(34b\)](#), we subtract the implicit half of the enthalpy gradient as before, but we also add two additional functions, each consisting of exactly one Chebyshev mode:

$$\hat{\mathbf{v}}^{N+1} = \hat{\mathbf{v}}^{N+\frac{3}{4}} - \hat{\mathbf{V}}^{N+1} \hat{\Pi}^{N+1} + \hat{\mathbf{z}}(\tau_1^{N+1} T_{M-1} + \tau_2^{N+1} T_M), \quad (\text{B.2})$$

where we have defined $\hat{\Pi} \equiv (\Delta t/2) \hat{h}$, and where τ_1 and τ_2 are scalars (as usual, we suppress the subscripts for wavenumber dependence). To find the enthalpy at the $N + 1$ step, we impose the anelastic constraint $\hat{\mathbf{V}}_A \cdot \hat{\mathbf{v}}^{N+1} = 0$, which yields:

$$\Delta_A^{N+1} \hat{\Pi}^{N+1} = \hat{\mathbf{V}}_A^{N+1} \cdot \hat{\mathbf{v}}^{N+\frac{3}{4}} + \tau_1^{N+1} D_A T_{M-1} + \tau_2^{N+1} D_A T_M, \quad (\text{B.3a})$$

$$D \hat{\Pi}^{N+1}(z = \pm 1) = \hat{v}_z^{N+\frac{3}{4}}(z = \pm 1) + \tau_1^{N+1} T_{M-1}(\pm 1) + \tau_2^{N+1} T_M(\pm 1). \quad (\text{B.3b})$$

We can break this up into three separate Poisson-like equations:

$$\hat{\Pi}^{N+1} = \hat{\Pi}_0^{N+1} + \tau_1^{N+1} \Gamma_1^{N+1} + \tau_2^{N+1} \Gamma_2^{N+1}, \quad (\text{B.4})$$

where Γ_1 and Γ_2 are Greens functions, and where:

$$\Delta_A^{N+1} \hat{\Pi}_0^{N+1} = \hat{\mathbf{V}}_A^{N+1} \cdot \hat{\mathbf{v}}^{N+\frac{3}{4}}, \quad (\text{B.5a})$$

$$D \hat{\Pi}_0^{N+1}(z = \pm 1) = \hat{v}_z^{N+\frac{3}{4}}(z = \pm 1), \quad (\text{B.5b})$$

$$\Delta_A^{N+1} \Gamma_1^{N+1} = D_A T_{M-1}, \quad (\text{B.5c})$$

$$D \Gamma_1^{N+1}(z = \pm 1) = T_{M-1}(\pm 1), \quad (\text{B.5d})$$

$$\Delta_A^{N+1} \Gamma_2^{N+1} = D_A T_M, \quad (\text{B.5e})$$

$$D \Gamma_2^{N+1}(z = \pm 1) = T_M(\pm 1). \quad (\text{B.5f})$$

Each of these three Poisson-like equations can be solved via the tau method as in [Appendix A](#). By construction, $\hat{\mathbf{V}}_A^{N+1} \cdot \hat{\mathbf{v}}^{N+1}$ equals zero for all Chebyshev modes except the two highest; for those modes, the values of the anelastic divergence are functions of τ_1^{N+1} and τ_2^{N+1} . We use these two degrees of freedom to impose that the anelastic divergence equal zero at the two highest modes as well, which yields the 2×2 matrix equation:

$$\begin{pmatrix} \alpha_{11} & \alpha_{12} \\ \alpha_{21} & \alpha_{22} \end{pmatrix} \begin{pmatrix} \tau_1^{N+1} \\ \tau_2^{N+1} \end{pmatrix} = \begin{pmatrix} \beta_1 \\ \beta_2 \end{pmatrix}, \quad (\text{B.6})$$

where we have defined:

$$\alpha_{11} \equiv [\Delta_A^{N+1} \Gamma_1^{N+1} - D_A T_{M-1}]|_{n=M-1}, \quad (\text{B.7a})$$

$$\alpha_{12} \equiv [\Delta_A^{N+1} \Gamma_2^{N+1} - D_A T_M]|_{n=M-1}, \quad (\text{B.7b})$$

$$\alpha_{21} \equiv [\Delta_A^{N+1} \Gamma_1^{N+1} - D_A T_{M-1}]|_{n=M}, \quad (\text{B.7c})$$

$$\alpha_{22} \equiv [\Delta_A^{N+1} \Gamma_2^{N+1} - D_A T_M]|_{n=M}, \quad (\text{B.7d})$$

$$\beta_1 \equiv [\hat{\mathbf{V}}_A^{N+1} \cdot \hat{\mathbf{v}}^{N+\frac{3}{4}} - \Delta_A^{N+1} \hat{I}_0^{N+1}]|_{n=M-1}, \quad (\text{B.7e})$$

$$\beta_2 \equiv [\hat{\mathbf{V}}_A^{N+1} \cdot \hat{\mathbf{v}}^{N+\frac{3}{4}} - \Delta_A^{N+1} \hat{I}_0^{N+1}]|_{n=M}, \quad (\text{B.7f})$$

where the notation $\hat{q}|_{n=M}$ represents the M th Chebyshev mode of function \hat{q} . Note that if M is even, then Γ_1^{N+1} is an even polynomial, Γ_2^{N+1} is an odd polynomial; if M is odd, then Γ_1^{N+1} is odd and Γ_2^{N+1} is even. Using these symmetries, one can show that $\alpha_{11} = \alpha_{22} = 0$, and $\tau_1^{N+1} = \beta_2/\alpha_{21}$, $\tau_2^{N+1} = \beta_1/\alpha_{12}$.

This method effectively triples the computational time for the enthalpy step (three Poisson-like solves instead of one per timestep). However, the enthalpy step is still only of order 10% of the total computational time, as the FFTs in the nonlinear advection dominate the computation. We also note that if we were not working in Lagrangian coordinates (which introduced explicit time dependence into the gradient operators), then the Greens functions Γ_1 and Γ_2 (two for each set of Fourier wavenumbers) would be independent of time, and would only have to be computed once in a pre-processing step, and stored.

Appendix C. Recursion relations for rational Chebyshev functions

Here we present some useful recursion relations for the rational Chebyshev functions. We define:

$$\begin{aligned} f(z) &= \sum_{n=0}^N \hat{f}_n^C C_n(z) \quad \text{or} \quad f(z) = \sum_{n=0}^N \hat{f}_n^S S_n(z), \\ g(z) &= \sum_{n=0}^N \hat{g}_n^C C_n(z) \quad \text{or} \quad g(z) = \sum_{n=0}^N \hat{g}_n^S S_n(z). \end{aligned} \quad (\text{C.1})$$

The first derivative operator converts a $C_n(z)$ series into a $S_n(z)$ series, and vice versa. The recursion relations have the same form for either case, except for the lowest two modes. Let $g = df/dz$, then:

$$\begin{aligned} \hat{g}_n^{S/C} &= [-(n-2)\hat{f}_{n-2}^{C/S} + 2n\hat{f}_n^{C/S} - (n+2)\hat{f}_{n+2}^{C/S}]/(4L_z), \quad \text{for } n \geq 2, \\ \hat{g}_0^S &= 0, \quad \hat{g}_1^S = (3\hat{f}_1^C - 3\hat{f}_3^C)/(4L_z), \quad \text{OR} \\ \hat{g}_0^C &= \hat{f}_2^S/(2L_z), \quad \hat{g}_1^C = (-\hat{f}_1^S + 3\hat{f}_3^S)/(4L_z). \end{aligned} \quad (\text{C.2})$$

The second derivative operator preserves the kind of expansion; that is, the second derivative of a $C_n(z)$ series is another $C_n(z)$ series, and the second derivative of a $S_n(z)$ series is another $S_n(z)$ series. The recursion relations for the second derivative operator have the same form for either case, except for the lowest four modes. Let $g = d^2f/dz^2$, then:

$$\begin{aligned}
 (16L_z^2)\hat{g}_n^{C/S} &= -(n-4)(n-2)\hat{f}_{n-4}^{C/S} + 4(n-2)(n-1)\hat{f}_{n-2}^{C/S} - 6n^2\hat{f}_n^{C/S} \\
 &\quad + 4(n+2)(n+1)\hat{f}_{n+2}^{C/S} - (n+4)(n+2)\hat{f}_{n+4}^{C/S} \quad \text{for } n \geq 4, \\
 \hat{g}_0^C &= [8\hat{f}_2^C - 8\hat{f}_4^C]/(16L_z^2), \\
 \hat{g}_1^C &= [-6\hat{f}_1^C + 21\hat{f}_3^C - 15\hat{f}_5^C]/(16L_z^2), \\
 \hat{g}_2^C &= [-24\hat{f}_2^C + 48\hat{f}_4^C - 24\hat{f}_6^C]/(16L_z^2), \\
 \hat{g}_3^C &= [9\hat{f}_1^C - 54\hat{f}_3^C + 80\hat{f}_5^C - 35\hat{f}_7^C]/(16L_z^2), \quad \text{OR} \\
 \hat{g}_0^S &= 0, \\
 \hat{g}_1^S &= [-6\hat{f}_1^S + 27\hat{f}_3^S - 15\hat{f}_5^S]/(16L_z^2), \\
 \hat{g}_2^S &= [-24\hat{f}_2^S + 48\hat{f}_4^S - 24\hat{f}_6^S]/(16L_z^2), \\
 \hat{g}_3^S &= [7\hat{f}_1^S - 54\hat{f}_3^S + 80\hat{f}_5^S - 35\hat{f}_7^S]/(16L_z^2).
 \end{aligned} \tag{C.3}$$

Like the second derivative operator, the $z(d/dz)$ operator preserves the kind of expansion. Let $g = z(df/dz)$, then:

$$\begin{aligned}
 \hat{g}_n^{C/S} &= [-(n-2)\hat{f}_{n-2}^{C/S} + (n+2)\hat{f}_{n+2}^{C/S}]/4 \quad \text{for } n \geq 2, \\
 \hat{g}_0^C &= \hat{f}_2^C/2, \quad \hat{g}_1^C = [\hat{f}_1^C + 3\hat{f}_3^C]/4, \quad \text{OR} \\
 \hat{g}_0^S &= 0, \quad \hat{g}_1^S = [-\hat{f}_1^S + 3\hat{f}_3^S]/4.
 \end{aligned} \tag{C.4}$$

One last important operation is multiplication by z . A simple recursion relation exists only for multiplication by z on a $S_n(z)$ series, which turns it into a $C_s(z)$ series. Let $g(z) = zf(z)$, then:

$$\hat{g}_n^C = \begin{cases} \sum_{\substack{k=2 \\ k \text{ even}}}^N \hat{f}_k^S & \text{for } n = 0, \\ \hat{f}_n^S + 2 \sum_{\substack{k=n \\ k \text{ even}}}^N \hat{f}_k^S & \text{for } n \text{ even,} \\ \hat{f}_n^S + 2 \sum_{\substack{k=n \\ k \text{ odd}}}^N \hat{f}_k^S & \text{for } n \text{ odd.} \end{cases} \tag{C.5}$$

In practice, the recursion relations for $z(d/dz)$ and d^2/dz^2 are unnecessary, as matrices for these operations can be built up from the first derivative matrices and the multiplication by z matrix.

References

- [1] F. Adams, R. Watkins, Vortices in circumstellar disks, *Astrophys. J.* 451 (1995) 314–327.
- [2] S. Balbus, J. Hawley, A powerful local shear instability in weakly magnetized disks. I. Linear analysis, *Astrophys. J.* 376 (1991) 214–222.
- [3] S. Balbus, J. Hawley, Instability, turbulence, and enhanced transport in accretion disks, *Rev. Mod. Phys.* 70 (1998) 1–53.
- [4] P. Bannon, On the anelastic approximation for a compressible atmosphere, *J. Atmos. Sci.* 53 (1996) 3618–3628.
- [5] P. Barge, J. Sommeria, Did planet formation begin inside persistent gaseous vortices? *Astron. Astrophys.* 295 (1995) L1–L4.
- [6] J. Barranco, P. Marcus, Vortices in protoplanetary disks and the formation of planetesimals, in: *Center for Turbulence Research – Proceedings of the 2000 Summer Program*, 2000, pp. 97–108.
- [7] J. Barranco, P. Marcus, Three-dimensional vortices in stratified protoplanetary disks, *Astrophys. J.* 623 (2005) 1157–1170.
- [8] J. Barranco, P. Marcus, M. Umurhan, Scalings and asymptotics of coherent vortices in protoplanetary disks, in: *Center for Turbulence Research – Proceedings of the 2000 Summer Program*, 2000, pp. 85–96.
- [9] O. Blaes, S. Balbus, Local shear instabilities in weakly ionized, weakly magnetized disks, *Astrophys. J.* 421 (1994) 163–177.
- [10] J. Boyd, Two comments on filtering (artificial viscosity) for Chebyshev and Legendre spectral and spectral element methods: preserving boundary conditions and interpretation of the filter as a diffusion, *J. Comput. Phys.* 143 (1998) 283–288.
- [11] J. Boyd, *Chebyshev and Fourier Spectral Methods*, Dover, Mineola, NY, 2000.
- [12] A. Cain, J. Ferziger, W. Reynolds, Discrete orthogonal function expansions for non-uniform grids using the fast Fourier transform, *J. Comput. Phys.* 56 (1984) 272–286.

- [13] C. Canuto, M. Hussaini, A. Quarteroni, T. Zang, Spectral Methods in Fluid Dynamics, Springer, New York, 1988.
- [14] S. Chandrasekhar, The stability of non-dissipative Couette flow in hydromagnetics, Proc. Natl. Acad. Sci. USA 46 (1960) 253–257.
- [15] S. Chandrasekhar, Hydrodynamic and Hydromagnetic Stability, Dover, New York, 1961.
- [16] J. Cho, M. de la Torre Juárez, A. Ingersoll, D. Dritschel, A high-resolution, three-dimensional model of Jupiter's Great Red Spot, J. Geophys. Res. 106 (2001) 5099–5105.
- [17] T. Dowling, A. Fischer, P. Gierasch, J. Harrington, R. Lebeau, C. Santori, The Explicit Planetary Isentropic-Coordinate (EPIC) atmospheric model, Icarus 132 (1998) 221–238.
- [18] D. Dritschel, M. Ambaum, A contour-advective semi-Lagrangian numerical algorithm for simulating fine-scale conservative dynamical fields, Q. J. R. Meteor. Soc. 123 (1997) 1097–1130.
- [19] C. Gammie, Layered accretion in T Tauri disks, Astrophys. J. 457 (1996) 355–362.
- [20] P. Gilman, G. Glatzmaier, Compressible convection in a rotating spherical shell. I. Anelastic equations, Astrophys. J., Suppl. Ser. 45 (1981) 335–349.
- [21] D. Givoli, Non-reflecting boundary conditions, J. Comput. Phys. 94 (1991) 1–29.
- [22] P. Goldreich, D. Lynden-Bell, I. Gravitational stability of uniformly rotating disks, Mon. Not. R. Astron. Soc. 130 (1965) 97–124.
- [23] D. Gottlieb, S. Orszag, Numerical Analysis of Spectral Methods: Theory and Applications, Society for Industrial and Applied Mathematics, Philadelphia, 1977.
- [24] D. Gough, The anelastic approximation for thermal convection, J. Atmos. Sci. 26 (1969) 448–456.
- [25] S. Kida, Motion of an elliptic vortex in a uniform shear flow, J. Phys. Soc. Jpn. 50 (10) (1981) 3517–3520.
- [26] D. Kosloff, H. Tal-Ezer, A modified Chebyshev pseudospectral method with an $o(n^{-1})$ time step restriction, J. Comput. Phys. 104 (1993) 457–469.
- [27] P. Kundu, Fluid Mechanics, Academic Press, San Diego, 1990.
- [28] C. Macaskill, W. Padden, D. Dritschel, The CASL algorithm for quasi-geostrophic flow in a cylinder, J. Comput. Phys. 188 (2003) 232–251.
- [29] P. Marcus, Simulation of Taylor–Couette flow. I. Numerical methods and comparison with experiment, J. Fluid Mech. 146 (1984) 45–64.
- [30] P. Marcus, Description and philosophy of spectral methods, in: K.-H. Winkler, M. Norman (Eds.), Proceedings of Astrophysical Radiation Hydrodynamics, Springer, Berlin, 1986, pp. 359–386.
- [31] P. Marcus, Vortex dynamics in a shearing zonal flow, J. Fluid Mech. 215 (1990) 393–430.
- [32] P. Marcus, Jupiter's Great Red Spot and other vortices, Annu. Rev. Astron. Astrophys. 31 (1993) 523–573.
- [33] P. Marcus, W. Press, On Green's functions for small disturbances of plane Couette flow, J. Fluid Mech. 79 (1977) 525–534.
- [34] M. Miesch, J. Elliott, J. Toomre, T. Clune, G. Glatzmaier, P. Gilman, Three-dimensional spherical simulations of solar convection. I. Differential rotation and pattern evolution achieved with laminar and turbulent states, Astrophys. J. 532 (2000) 593–615.
- [35] A. Mohebalhojeh, D. Dritschel, Contour-advective semi-Lagrangian numerical algorithms for many-layer primitive equation models, Q. J. R. Meteor. Soc. 130 (2004) 347–364.
- [36] D. Moore, P. Saffman, Structure of a line vortex in an imposed strain, in: J.H. Olsen, A. Goldburg, H. Rogers (Eds.), Aircraft Wake Turbulence and its Detection, Plenum Press, New York, 1971, pp. 339–354.
- [37] Y. Ogura, N. Phillips, Scale analysis of deep and shallow convection in the atmosphere, J. Atmos. Sci. 19 (1962) 73–79.
- [38] J. Pedlosky, Geophysical Fluid Dynamics, Springer, New York, 1979.
- [39] R. Rogallo, Numerical experiments in homogeneous turbulence, Technical memorandum 81315, NASA, 1981.
- [40] J. Stone, 2006. Available from: <<http://www.astro.princeton.edu/~jstone/athena.html>>.
- [41] J. Stone, M. Norman, ZEUS-2D: a radiation magnetohydrodynamics code for astrophysical flows in two space dimensions: I. The hydrodynamic algorithms and tests, Astrophys. J., Suppl. Ser. 80 (1992) 753.
- [42] J. Stone, M. Norman, ZEUS-2D: A radiation magnetohydrodynamics code for astrophysical flows in two space dimensions: II. The magnetohydrodynamic algorithms and tests, Astrophys. J., Suppl. Ser. 80 (1992) 791.
- [43] J. Stone, M. Norman, ZEUS-2D: a radiation magnetohydrodynamics code for astrophysical flows in two space dimensions: III. The radiation hydrodynamic algorithms and tests, Astrophys. J., Suppl. Ser. 80 (1992) 819.
- [44] E. Velikhov, Stability of an ideally conducting liquid flowing between cylinders rotating in a magnetic field, Sov. Phys. JETP 36 (1959) 1398–1404.